

Silicate Weathering in the Semi-Arid Southern Pyrenees During the PETM: Lithium Isotope Evidence

Rocio Jaimes-Gutierrez¹, Marine Prieur¹, David J. Wilson², Philip A.E. Pogge von Strandmann^{2,3}, Emmanuelle Pucéat⁴, Thierry Adatte⁵, Jorge E. Spangenberg⁶, Sébastien Castelltort¹

¹ Department of Earth Sciences, University of Geneva, Rue des Maraichers 13, 1205, Geneva, Switzerland

² London Geochemistry and Isotope Centre (LOGIC), Institute of Earth and Planetary Sciences, University College London and Birkbeck, University of London, Gower Street, London WC1E 6BT, UK

³ Institute of Geosciences, Johannes Gutenberg University Mainz, Mainz, Germany

⁴ Biogéosciences Dijon, Université Bourgogne Franche – Comté, UMR CNRS 6282, Dijon, France.

⁵ Institute of Earth Sciences, Géopolis, University of Lausanne, 1015 Lausanne, Switzerland

⁶ Institute of Earth Surface Dynamics, Géopolis, University of Lausanne, 1015 Lausanne, Switzerland

Correspondence to: Rocio Jaimes-Gutierrez, Rocio.JaimesGutierrez@unige.ch

Abstract

The Palaeocene-Eocene Thermal Maximum (PETM), a hyperthermal event ~56 Ma ago, allows the Earth system response to abrupt climate change to be explored. Recent investigations link the PETM with a negative lithium isotope ($\delta^7\text{Li}$) excursion, interpreted as an increase in continental silicate weathering fluxes, which can regulate Earth's surface temperature over geological timescales. However, the silicate weathering response under different climatic regimes has yet to be constrained. Here we aim to address the chemical weathering response to the PETM in the semi-arid Southern Pyrenees, and to explore how different archives (i.e. clays and carbonate nodules) record the weathering changes.

We investigated two continental sections in the southern Pyrenees. In the Esplugafreda section, we measured $\delta^7\text{Li}$ values as a silicate weathering proxy and ϵ_{Nd} values as a provenance proxy in the clay minerals. In the Rin section, we characterised the PETM locally by analysing $\delta^{13}\text{C}$ values in organic matter and examined the clay mineralogy in the paleosols, as well as measuring $\delta^7\text{Li}$ values in clays and carbonate nodules to trace silicate weathering. In the Esplugafreda section, we observe temporally stable ϵ_{Nd} values, while the $\delta^7\text{Li}_{\text{clays}}$ record shows two small positive excursions, one during the Pre-Onset Excursion (~0.7‰) and a second during the body of the PETM (~0.8‰). In the Rin section, the PETM is characterised by a negative carbon isotope excursion of 2.8‰. The clays consist mostly of illite/smectite, illite, kaolinite, and chlorite consistent with a seasonal climate in the region, and we find a positive $\delta^7\text{Li}_{\text{clays}}$ excursion of ~0.8‰.

The combined $\delta^7\text{Li}_{\text{clays}}$ and ϵ_{Nd} records indicate increased clay formation and increased silicate weathering fluxes in the semi-arid Pyrenees, while the sediment provenance was stable. The $\delta^7\text{Li}$ values in the carbonate nodules indicate more variability, potentially due to clay contamination. Constrained by the bedrock type of dominantly reworked sediments and the seasonal precipitation regime, the initially low weathering fluxes, despite a comparatively high weathering intensity, evolved towards higher weathering fluxes with enhanced erosion during the PETM.

Short Summary

How do semi-arid landscapes respond to rapid global warming? During the PETM – an extreme warming event 56 Ma ago – global lithium isotope records show a negative $\delta^7\text{Li}$ excursion, suggesting an increase in weathering fluxes. In the Southern Pyrenees, however, we find the opposite signal: clay $\delta^7\text{Li}$ values became ~1‰ heavier, indicating enhanced clay formation. These results suggest that regional hydroclimatic conditions can decouple terrestrial signals from global averages.

1. Introduction

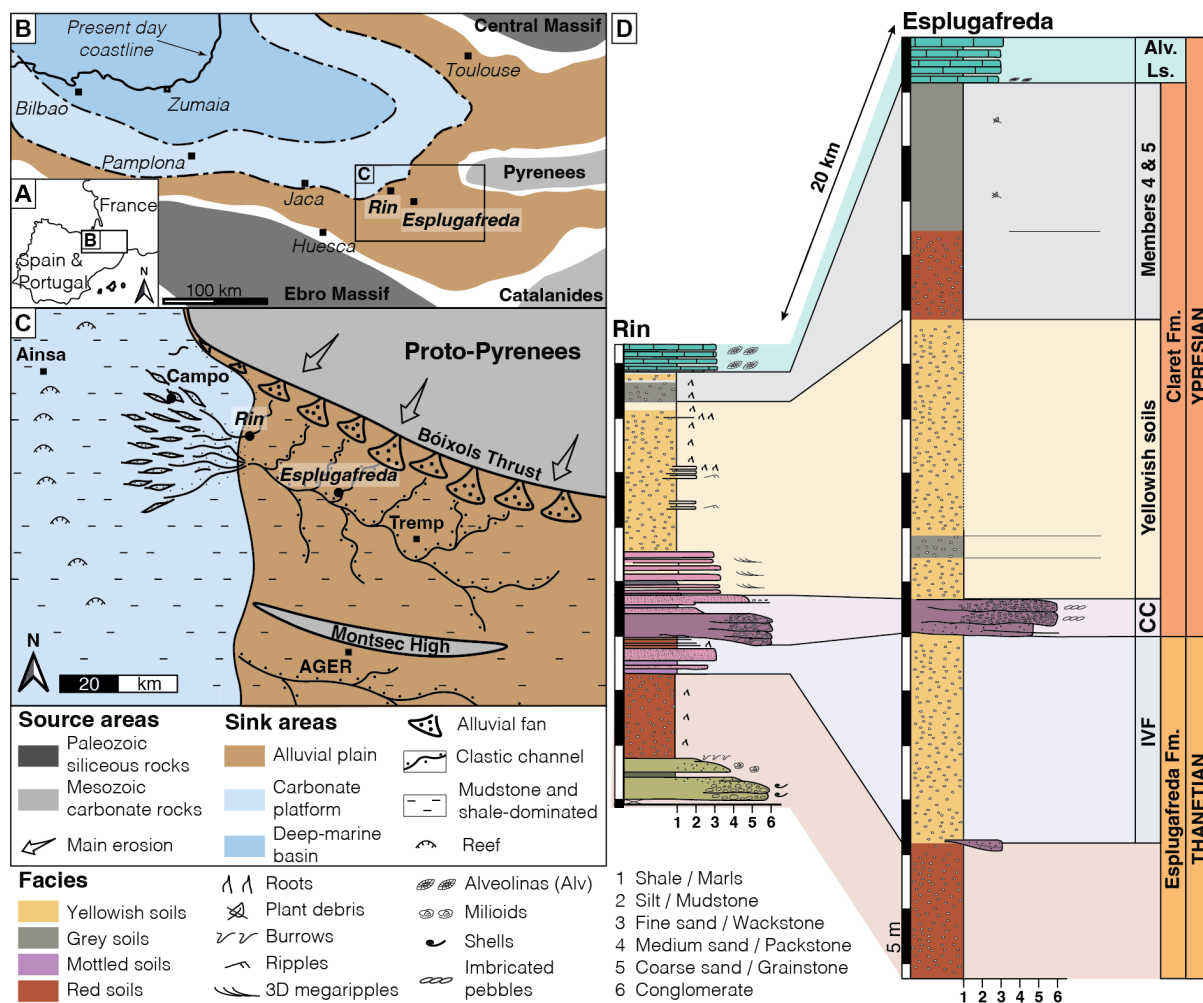
Continental silicate weathering is a critical feedback mechanism that stabilises Earth's climate over geological timescales by regulating atmospheric CO₂ through the long-term carbon cycle (Walker et al., 1981; Raymo and Ruddiman, 1992; Maher and Von Blanckenburg, 2023). Through the breakdown of silicate minerals, the transport of cations in river systems, and the precipitation and burial of carbonates in the ocean, silicate weathering sequesters atmospheric CO₂, acting as a natural climate thermostat. Understanding how this process responds to abrupt climate change is essential for evaluating its capacity to modulate carbon fluxes under a range of future warming scenarios.

The Palaeocene-Eocene Thermal Maximum (PETM), a hyperthermal event ~56 Ma ago, resulted from the rapid release of greenhouse gases that triggered a 5–8 °C global temperature increase over a geologically brief interval (Kennett and Stott, 1991; Dickens et al., 1995; Zachos et al., 2003, 2008; Westerhold et al., 2009; McInerney and Wing, 2011). Global records from the PETM suggest increases in silicate weathering fluxes (e.g. Hessler et al., 2017; Pogge von Strandmann et al., 2021; Jaimes-Gutierrez et al., 2025; Rush et al., 2025), while some local records have been interpreted to show increased weathering intensity (e.g. Ramos et al., 2022; Chen et al., 2023), underscoring the potential for weathering to buffer atmospheric CO₂ during extreme warming events. In the context of modern anthropogenic warming, these insights are crucial for understanding the capacity of natural systems to mitigate rising CO₂ levels (Zeebe et al., 2016; Carmichael et al., 2017 and references therein).

In mid-latitude records, a range of sedimentological, geochemical, and mineralogical proxies suggest that the PETM resulted in a hydrological perturbation with episodic extreme rainfall events, increased seasonality, and aridification, leading to a loss of vegetation, extreme flooding, and enhanced channel mobility (Schmitz et al., 2001; Schmitz and Pujalte, 2007; Carmichael et al., 2017; Chen et al., 2018; Rush et al., 2021; Barefoot et al., 2022; Vimpere et al., 2023). These changes were particularly pronounced in semi-arid regions such as the Southern Pyrenees (~35°N paleolatitude, **Fig. 1**), where sedimentary records document hydrological seasonality, enhanced erosion, and increased sediment transport (Schmitz and Pujalte, 2007; Pujalte et al., 2015; Chen et al., 2018; Rush et al., 2021; Prieur et al., 2024, 2025; Jaimes-Gutierrez et al., 2024).

The Southern Pyrenees (**Fig. 1**) offer an exceptional setting for investigating climate-driven weathering dynamics. This region experienced tectonic quiescence during the PETM (Rosenbaum et al., 2002), allowing for the isolation of the effects of climate and hydrology on weathering. Sedimentary records indicate enhanced hydrological seasonality and increased runoff, consistent with amplified denudation rates during this interval (Schmitz and Pujalte, 2007; Pujalte et al., 2015; Rush et al., 2021). In this study, we use lithium isotopes ($\delta^7\text{Li}$) as a proxy for silicate weathering and neodymium isotopes (ϵ_{Nd}) as a tracer for sediment provenance, in order to quantify the weathering responses in the Southern Pyrenees and to assess their regional contribution to CO₂ regulation during the PETM.

We focus on two continental floodplain sections to answer two primary questions: (i) What was the chemical weathering response to the PETM in the semi-arid Southern Pyrenees? (ii) How do different sedimentary archives, such as clays and carbonate nodules, record the weathering changes? In the Esplugafreda section, we measured $\delta^7\text{Li}$ values in clay minerals as a weathering proxy, together with ϵ_{Nd} values in two clay size fractions to determine sediment provenance. In the Rin section, we characterised the PETM locally through $\delta^{13}\text{C}$ measurements in organic matter, and analysed the clay mineralogy of paleosols, and $\delta^7\text{Li}$ values in both clays and carbonate nodules. These geochemical and mineralogical datasets allow us to reconstruct weathering dynamics in the region and to assess how they compare with existing globally-distributed records of PETM weathering (Pogge von Strandmann et al., 2021b; Ramos et al., 2022; Chen et al., 2023; Jaimes-Gutierrez et al., 2025; Rush et al., 2025).



97
 98 **Figure 1.** (A) Location map. (B) Palaeogeography of the Tremp-Graus Basin during the late Palaeocene, modified
 99 after Jaimes-Gutierrez et al. (2024) and references therein. (C) Sediment routing system during the late
 100 Palaeocene, with the floodplain Esplugafreda section and the more coastal Rin section, at the marine-continent
 101 transition, modified from Prieur et al. (2025). (D) Stratigraphy and correlation between the Esplugafreda and
 102 Rin terrestrial sections. CC, Claret Conglomerate. Alv. Ls., Alveolina Limestone.

103 1.1. Silicate weathering as Earth's surface thermostat

104 Silicate weathering rates are influenced by climate (Dessert et al., 2003; West et al., 2005), vegetation (Moulton
 105 et al., 2000; Porder, 2019), lithology (Dessert et al., 2003; Caves et al., 2016; Murray and Jagoutz, 2024), and
 106 regolith properties (Kump and Arthur, 1997; Caves Rügenstein et al., 2019). Weathering is driven by the
 107 availability of fresh mineral surfaces, reactive fluids, and dissolution kinetics (Riebe et al., 2004; Bufe et al., 2021;
 108 Maher and Von Blanckenburg, 2023). Denudation ($D = \text{erosion rate } [E] + \text{silicate weathering } [W]$) links surface
 109 processes to the carbon cycle because erosion supplies fresh minerals, enhancing CO₂ sequestration through
 110 chemical weathering (Gaillardet et al., 1999; Riebe et al., 2004; West et al., 2005; Anderson et al., 2007; Hilton,
 111 2023).

112 Two end-member regimes can be used to describe chemical weathering dynamics. In supply-limited regimes,
 113 mature soils dominated by secondary clays shield bedrock, limiting fresh mineral exposure and resulting in low
 114 weathering rates (Goddéris et al., 2008). In kinetically-limited regimes, which are typical of high-relief areas with
 115 thin soils, weathering rates are controlled by mineral dissolution kinetics (Kump et al., 2000; Riebe et al., 2004;
 116 West et al., 2005). Investigating how climate and erosion interact to shape these regimes under hyperthermal
 117 events such as the PETM is thus essential for understanding the weathering mechanisms and rates underpinning
 118 Earth's carbon cycle feedbacks in a warming climate.

119 **1.2. Lithium isotopes as a chemical weathering tracer**

120 Secondary clay minerals, which form as a by-product of primary silicate rock dissolution, preferentially
121 incorporate ${}^6\text{Li}$ over ${}^7\text{Li}$, resulting in isotopically light clays and isotopically heavy waters (e.g. Pogge von
122 Strandmann et al., 2020). As weathering progresses, both dissolved lithium and the clays that precipitate from it
123 become isotopically heavier, with the $\delta^7\text{Li}$ value of the water and soil being linked by an approximately constant
124 fractionation factor (Pogge von Strandmann et al., 2021a). Measuring $\delta^7\text{Li}$ values in detrital and carbonate
125 archives therefore allows past weathering regimes to be reconstructed. Because carbonate weathering has a
126 minimal influence on riverine lithium budgets, $\delta^7\text{Li}$ variations primarily reflect silicate weathering processes
127 (Kisakürek et al., 2005). Consequently, lithium isotopes have become widely applied as a proxy for tracking clay
128 mineral formation, and thereby tracing silicate weathering intensity changes, both in modern systems (e.g.
129 Dellinger et al., 2015, 2017; Pogge von Strandmann et al., 2023) and during past geological events (e.g. Misra
130 and Froelich, 2012; Pogge von Strandmann et al., 2013, 2021; Ramos et al., 2022; Jones et al., 2023).

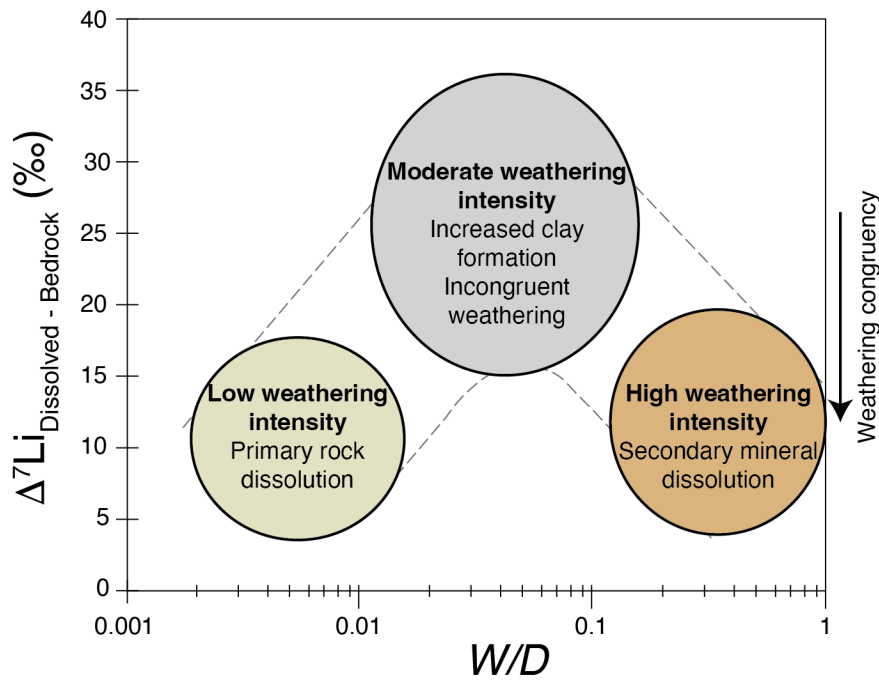
131
132 Weathering congruency, which represents the balance between primary mineral dissolution and secondary clay
133 mineral formation, determines the $\delta^7\text{Li}$ composition of river waters and sediments (Dellinger et al., 2015; Zhang
134 et al., 2022 and references therein). In rapidly eroding regions with low W/D , congruent weathering results in
135 minimal isotopic fractionation, because clay formation is relatively low (**Fig. 2**). In contrast, incongruent
136 weathering in soil-mantled environments with moderate W/D , such as floodplains with high clay formation, yields
137 both clays and waters with higher $\delta^7\text{Li}$ values (**Fig. 2 and 3**). Finally, in supply-limited regimes with high W/D ,
138 such as rainforests, there is no remaining primary rock material to weather, so pre-formed clays are re-dissolved,
139 which drives solutions to low $\delta^7\text{Li}$ values, but with a very low weathering flux (e.g. Dellinger et al., 2015). In
140 modern rivers, clays take up their Li from solution with an approximately constant fractionation factor (Pistiner
141 and Henderson, 2003; Pogge von Strandmann et al., 2023; Ramos et al., 2024), so their composition also mimics
142 this boomerang curve (Winnick et al., 2022; Pogge von Strandmann et al., 2023; Wei et al., 2025).

143
144 In detrital sediment archives, only part of this boomerang trend is typically observed because of mixing of the
145 neoformed clays with primary silicate material, especially at low W/D conditions (Dellinger et al., 2017).
146 Therefore, continental and marine detrital records may need to be interpreted differently (e.g. Pogge von
147 Strandmann et al., 2021; Ramos et al., 2022, 2024; Jones et al., 2023; Jaimes-Gutierrez et al., 2025; Rush et al.,
148 2025; Wei et al., 2025). Because finer sediment fractions tend to be preferentially transported further offshore due
149 to hydrodynamic sorting during river to marine transport, clay-sized records may be more clearly expressed in
150 some marine sedimentary records (e.g. Gibbs, 1977; Liu et al., 2023). Such biases resulting from mixing with
151 primary silicate grains in bulk sediment samples can potentially be reduced by analysing the clay size fraction (<2
152 μm), although this fraction can still also contain some primary minerals.

153
154 Finally, lithium isotopes can also be fractionated by direct climatic fluctuations. For example, temperature (Vigier
155 et al., 2008; Li and West, 2014) and hydrological controls (Zhang et al., 2022) have both been found to influence
156 the $\delta^7\text{Li}$ composition of river water, and consequently the composition of the sedimentary archives that form in
157 equilibrium with them (Pogge von Strandmann et al., 2023). In particular, riverine dissolved $\delta^7\text{Li}$ values have
158 been shown to have a negative correlation with runoff, because it controls the water-rock residence time that
159 affects clay formation, with the dry season exhibiting enhanced clay formation and higher $\delta^7\text{Li}$ values than the
160 wet season (Wilson et al., 2021; Zhang et al., 2022).

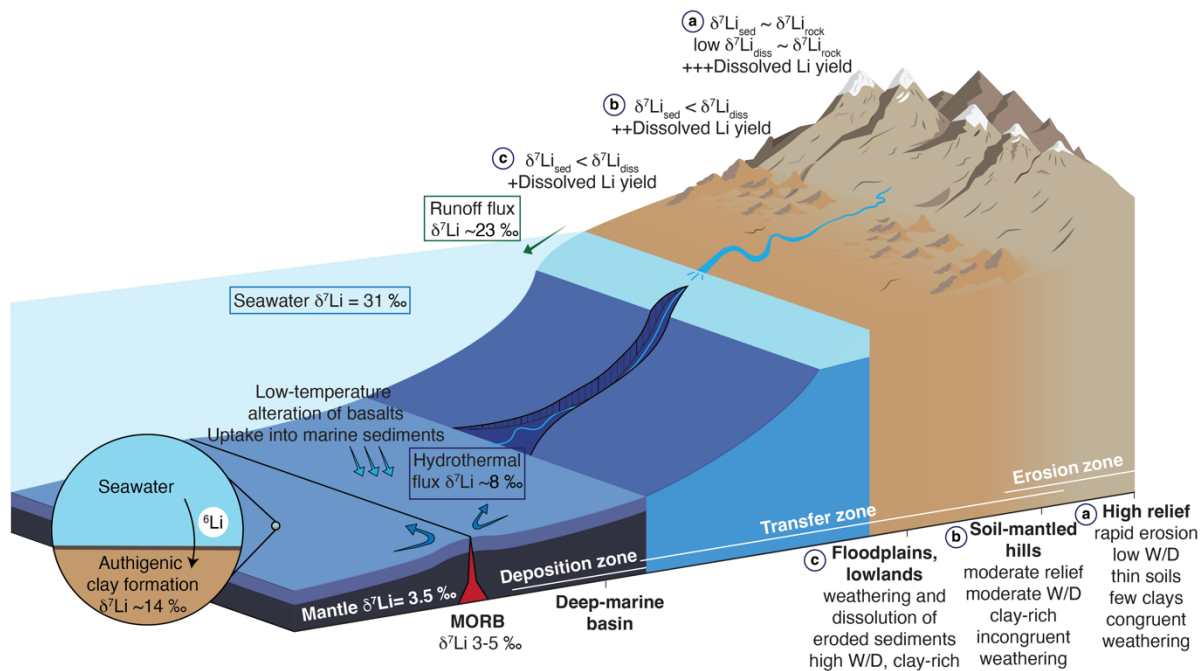
161
162 A detailed discussion on the lithium isotope interpretative framework, including the roles of grain size,
163 hydrodynamic sorting, and lithology, is provided in Jaimes-Gutierrez et al. (2025, Supplemental Material).

164



165
 166 **Figure 2.** Large-river dissolved lithium isotope composition ($\delta^7\text{Li}_{\text{dissolved}}$) corrected for bedrock composition
 167 ($\Delta^7\text{Li}_{\text{dissolved-bedrock}}$) plotted versus weathering intensity (W/D). Modified from Dellinger et al. (2015) and references
 168 therein.
 169

170 During the PETM, Pogge von Strandmann et al. (2021) documented a $\sim 3\text{‰}$ negative $\delta^7\text{Li}$ excursion in several
 171 marine carbonate sections, indicating globally enhanced weathering fluxes (50–60%) and erosion rates (2–3x),
 172 and a shift to an overall lower weathering intensity regime. At a continental scale, detrital lithium isotope records
 173 from North America show coherent negative $\delta^7\text{Li}$ excursions in both floodplain and deep-marine settings,
 174 indicating rapid propagation of erosion- and weathering-related signals through sediment-routing systems under
 175 intensified hydrological conditions, despite largely stable sediment provenance (Ramos et al., 2022; Jaimes-
 176 Gutierrez et al., 2025; Rush et al., 2025). On a regional scale, Ramos et al. (2022) reported a rapid, sustained
 177 increase in silicate weathering intensity in the Bighorn Basin floodplains that was attributed to seasonal
 178 hydrological variability. Similarly, Chen et al. (2023) identified a $\sim 100\%$ increase in silicate weathering intensity
 179 in the Nanyang Basin, East Asia. These studies highlight the roles of local hydrology, lithology, and erosion in
 180 shaping regional weathering responses and the associated $\delta^7\text{Li}$ changes. However, they also reveal significant
 181 gaps in our understanding of how regional processes integrate into driving global $\delta^7\text{Li}$ records and carbon cycle
 182 feedbacks. Notably, discrepancies between the proposed increases in weathering intensity at a regional scale
 183 (Ramos et al., 2022; Chen et al., 2023) and the inferred decrease at a global scale (Pogge von Strandmann et al.,
 184 2021b; Jaimes-Gutierrez et al., 2025; Rush et al., 2025) require further assessment of how regional climatic and
 185 geological controls translate into weathering responses.
 186



187
 188 **Figure 3.** Processes determining the lithium isotope composition of bulk sediments ($\delta^7\text{Li}_{\text{sed}}$) and dissolved lithium
 189 flux along a sediment routing system from source to sink in relation to denudation. The weathering intensity (W/D)
 190 expresses the relative share of weathering (W) over denudation (D), where $D = W + E$ (erosion). Modified from
 191 Tofelde et al. (2021), Pogge von Strandmann et al. (2021a), and Bufer et al. (2024).
 192

193 To address these gaps, we focused on the silicate weathering response to the PETM climatic perturbation in two
 194 sections of the Southern Pyrenees (Espugafreda and Rin, **Fig. 1**). With its semi-arid climate, seasonal precipitation,
 195 and relatively unreactive lithologies comprising reworked sediments and significant carbonate content (e.g.
 196 Eichenseer, 1988; Eichenseer and Luterbacher, 1992; Gómez-Gras et al., 2016), this setting represents a
 197 contrasting regional weathering regime to previous PETM studies. Our results contribute to understanding how
 198 floodplain paleosols, which are often overlooked in global weathering studies, respond to climatic perturbations,
 199 with broader implications for the recovery of Earth's climate system after significant warming events.

200 2. Geological context

201 The Pyrenees formed as a result of convergence between the Iberian and European plates, a process that initiated
 202 in the Late Cretaceous and continued into the Miocene (Mattauer and Henry, 1974; Roure et al., 1989; Roest and
 203 Srivastava, 1991; Rosenbaum et al., 2002). The orogenic evolution began with the mid-Cretaceous hyper-
 204 extension of the Iberian margins, followed by the late Cretaceous subduction and collision with the European
 205 plate (Teixell et al., 2016). Foreland basins formed on both sides of the fold and thrust belt (Puigdefbregas and
 206 Souquet, 1986; Muñoz, 1992; Gómez-Gras et al., 2016). The Southern Pyrenean foreland basin was active
 207 between the Late Cretaceous and the Oligocene, and contains well-preserved sedimentary archives of continental
 208 and marine environments.
 209

210 The Tremp-Graus Basin is located in the South-Central Pyrenean Foreland Basin (Spain), delimited by the Boixols
 211 Thrust to the north and the Montsec Thrust to the south (**Fig. 1C**). During the Palaeocene, the Tremp-Graus Basin
 212 was dominated by continental sedimentation sourced from the Pyrenees (Gómez-Gras et al., 2016). The
 213 continental deposits of the Thanetian Esplugafreda Formation (Fm.) predominantly represent floodplain sediment
 214 accumulation and consist of clay, silt, carbonate nodules, and *Microcodium* grains, with some isolated sandy to
 215 conglomeratic channels (Puigdefbregas and Souquet, 1986; Dreyer, 1993; Schmitz and Pujalte, 2003, 2007).

216 2.1. Esplugafreda section

217 The Esplugafreda section (42°14'50" N; 0°45'13" E, **Fig. 1B**) has been widely studied for its well-preserved
 218 Palaeocene-Eocene sedimentary record (Schmitz and Pujalte, 2003; Baceta et al., 2005; Khozyem, 2013; Tremblin
 219 et al., 2022; Basilici et al., 2022; Jaimes-Gutierrez et al., 2024) (**Fig. 1D**). The Upper Thanetian sediments belong
 220 to the Esplugafreda Fm. in the Tremp Group of the Tremp-Graus Basin (Dreyer, 1993). This formation consists
 221 of coarse-grained stream deposits intercalated with red floodplain sediments that are rich in carbonate nodules
 222 and characterised by mature paleosols. The PETM sediments have been classified into five stratigraphic members

223 (Pujalte and Schmitz, 2005; Pujalte et al., 2014; Colombera et al., 2017; Basilici et al., 2022). Member 1 belongs
 224 to the Esplugafreda Fm. and consists of a fining-upwards sequence of conglomerates and cross-laminated
 225 sandstones, known as the Incised Valley Fill (IVF) sediments. During this interval, a first negative carbon isotope
 226 excursion (CIE) marks the Pre-Onset Excursion (POE) (Khozyem, 2013; Tremblin et al., 2022). Member 2 at the
 227 onset of the Ypresian is represented by the Claret Conglomerate (Pujalte and Schmitz, 2005), a 3-5 m thick
 228 conglomeratic unit, corresponding to a braid plain which has been interpreted as the proximal part of a megafan
 229 (Schmitz and Pujalte, 2007). Member 3, the Yellowish soils, consists of yellow mudstone with purple mottling,
 230 and the main body of the CIE is recorded during this interval (Pujalte and Schmitz, 2005). Member 4, consisting
 231 of red soil with gypsum, and Member 5, comprising light red mudstones with scarce carbonate nodules,
 232 correspond to the recovery interval of the PETM in this locality (Pujalte and Schmitz, 2005; Baceta et al., 2011;
 233 Khozyem, 2013; Pujalte et al., 2014; Tremblin et al., 2022; Basilici et al., 2022).

234 2.2. Rin section

235 The Rin section (42°19'42.01"N; 0°32'42.16"E, **Fig. 1B and Fig. 4**) is a Palaeocene-Eocene sequence comprising
 236 mudstone-dominated alluvial deposits and very shallow marine carbonate alternations, indicating episodes of
 237 transgression and regression on the coastal plain (Schmitz and Pujalte, 2007) (**Fig. 1**). The upper Esplugafreda
 238 Fm. soils are characterised by grey mottling and sparse iron nodules, with preserved pedogenic features such as
 239 peds. Member 1, the IVF, consists of 4 m-thick reddish-yellow soils that are rich in carbonate nodules. Member
 240 2, the Claret Conglomerate, outcrops as a 3 m-thick calcareous conglomerate with pale red clay pockets, and has
 241 sparse carbonate nodules and charophyte occurrences. Member 3, the Yellowish soils, consists of 13 m-thick
 242 reddish-yellow clays and silts. The base of Member 3 records sparse occurrences of lignite and carbonate nodules.
 243 Member 4 is not preserved in the Rin section, and the upper 3 m of the sequence consists of Member 5, which has
 244 light grey to reddish yellow soils with grey mottling, before the overlying Alveolina Limestone.
 245



246 **Figure 4.** Rin section between the upper Thanetian and lower Ypresian. Members 1-5 described in the literature
 247 for the Esplugafreda section can be identified in the Rin section, except that Member 4 from the recovery phase
 248 of the PETM has not been preserved. E. Fm.: Esplugafreda Formation.
 249

250 3. Material and methods

251 3.1. Size fraction separation

252 Standard protocols (e.g. Adatte et al., 1996; Bauer et al., 2016) were followed for decarbonation and size fraction
 253 separation at the Institute of Earth Sciences clay laboratory at the University of Lausanne (ISTE-UNIL). Samples
 254 (~5 g) were leached with 10% HCl for 30 min in a bubble bath, including 3 min in an ultrasonic bath, to
 255 disaggregate sediments and dissolve calcite. Distilled water was used to remove the acid until a neutral pH was
 256 obtained. Subsequently, the <2 µm fraction was separated by settling and enhanced with a centrifuge. Settling and
 257 extraction were repeated three times.

258 3.2. Clay mineralogy

259 The clay minerals were identified on air-dried and ethylene glycol-solvated samples at ISTE-UNIL following the
 260 protocol described in Adatte et al. (1996). An aliquot of the separated size fractions was pipetted on glass slides
 261 and dried at room temperature. The air-dried samples were further analysed with a Thermo Scientific ARL X'TRA
 262 powder diffractometer equipped with a Cu anode, operated at 45 kV and 40 mA. The step size was 0.02 °, with a
 263 scan rate of 0.5-1.2 °/min. Samples were glycolated to identify smectite (Moore and Reynolds, 1992).
 264 Diffractograms were analysed using the XRDWin software, where the background was removed, and a
 265 deconvolution was performed for overlapping peaks (e.g. K002 and Ch004).

266 3.3. Nodule purification

267 Carbonate nodules were washed with running distilled water until visible clay clumps were removed. They were
268 then placed in a beaker with distilled water and in an ultrasonic bath to remove the remaining clay particles. A
269 second round in the ultrasonic bath was then carried out with some drops of 10 M HCl in order to remove the
270 outermost layer. The nodules were later washed in running distilled water, dried at 40 °C, and ground.

271 3.4. Rock-Eval pyrolysis

272 Organic matter analyses were performed on powdered bulk rock samples using a Rock-Eval 6 at ISTE-UNIL,
273 following standard methodology (Espitalie et al., 1985; Behar et al., 2001). For calibration, the IFP 160000
274 standard was used. The Rock-Eval pyrolysis parameters measured were hydrogen index (HI, mg HC/g TOC, HC
275 = hydrocarbons), oxygen index (OI, mg CO₂/g TOC), Tmax (°C), and total organic carbon content (TOC, wt.%).
276 The HI, OI, and Tmax values give an overall measurement of the type and degree of maturation of the organic
277 matter (e.g. Espitalie et al., 1985).

278 3.5. Isotope geochemistry

279 3.5.1. Organic matter carbon isotopes

280 The carbon isotope composition of the decarbonated bulk rock samples was determined at the Institute of Earth
281 Surface Dynamics at the University of Lausanne (IDYST-UNIL) by elemental analysis/isotope ratio mass
282 spectrometry (EA/IRMS). The EA/IRMS system consisted of a Carlo Erba 1108 (Fisons Instruments, Milan, Italy)
283 elemental analyser connected to a Delta V Plus isotope ratio mass spectrometer via a ConFlo III split interface
284 (both Thermo Fisher Scientific, Bremen, Germany) operated under continuous helium (He) flow (Spangenberg,
285 2006; Spangenberg and Zufferey, 2019). The carbon isotope compositions were reported in the delta (δ) notation
286 as permil (‰) variations of the molar ratio of the heavy to light isotope (¹³C/¹²C) relative to the international
287 standard Vienna Pee Dee Belemnite limestone (VPDB). For calibration and normalisation of the measured δ¹³C
288 values to the Vienna Pee Dee Belemnite limestone (VPDB) standard, a four-point calibration was used with
289 international reference materials and in-house standards (Spangenberg and Zufferey, 2019). The used standards
290 included UNIL-Glycine (δ¹³C = -26.10 ± 0.05‰), UNIL-Urea-1 (δ¹³C = -43.00 ± 0.04‰), UNIL-Pyridine (δ¹³C
291 = -29.25 ± 0.06‰), and the RM USGS24 graphite (δ¹³C = -16.05 ± 0.04‰). Analyses were done in duplicates.
292 The accuracy of the analyses was checked periodically through the analysis of international RM standards not
293 used for calibration. The reproducibility and precision of the EA/IRMS δ¹³C analyses were determined by the
294 standard deviation of separately replicated analyses and were better than 0.1‰.

295 3.5.2. Lithium isotopes

296 Sample digestion, column chemistry, and mass spectrometry were conducted in the London Geochemistry and
297 Isotope Centre (LOGIC) laboratories at University College London (UCL) and Birkbeck, University of London.
298 Clay samples were subjected to bulk digestion using concentrated HF, HNO₃, and HClO₄ in Teflon beakers on a
299 hot plate at 130 °C, followed by steps in concentrated HNO₃ and 6 M HCl. The carbonate nodules were subject
300 to leaching to separate the carbonate and detrital fractions. The carbonate fraction was extracted by leaching ~100
301 mg of sample in 8 ml 0.1 M HCl for 1 h (Pogge von Strandmann et al., 2013; Wilson et al., 2021), allowing a
302 maximum of ~40 mg of calcium carbonate to be dissolved.

303 A standard method of elution was applied for lithium isotope separation in 0.2 M HCl. Two-column passes were
304 applied through AG50W-X12 resin to ensure matrix removal (Pogge von Strandmann et al., 2013). Given that
305 lithium isotopes are fractionated during ion chromatography, sample splits were collected before and after the
306 lithium collection interval to assess column yields. For example, a 1% loss in yield at UCL has been assessed to
307 lead to an offset of 1.7‰ (Wilson et al., 2021). Here, yields between two column passes were 99.8-100%,
308 indicating excellent recovery.

309
310 Lithium isotope measurements were performed on a Nu Plasma 3 MC-ICP-MS at UCL, using a Cetac Aridus 2
311 desolvation system, ‘super-lithium’ cones, and standard-sample bracketing with the IRMM-016 Li standard
312 (Pogge von Strandmann et al., 2019). Samples were measured at least three times within an analytical session,
313 with each measurement integrating ~50 s, and the reported values are the mean and standard deviation (2sd) of
314 these values, given in permil (‰) relative to the IRMM-016 standard. Accuracy and external reproducibility were
315 assessed using seawater and USGS standard BCR-2, which gave δ⁷Li values of +31.3 ± 0.6‰ (2sd, n = 28) and
316 +2.5 ± 0.3‰ (n = 5), respectively.

318 3.5.3. Neodymium isotopes and rare earth element concentrations

319 After decarbonation using 10% HCl for 30 min, clays were separated from decarbonated sediments into <0.5 μm
320 and 0.5-2 μm fractions (analytical protocol for size fraction separation reported in Jaimes-Gutierrez et al., 2024).
321 A total of 18 samples (8 in the <0.5 μm size fraction and 10 in the 0.5-2 μm size fraction) were analysed for their
322 neodymium (Nd) isotopic composition and their Nd and samarium (Sm) concentrations. Aliquots of about 1.5 mg
323 of each clay fraction followed a sequential leaching procedure to remove Fe-Mn oxides and organic matter, based
324 on the protocol of Bayon et al. (2002) and Gutjahr et al. (2007), slightly adapted. The Fe-Mn oxides were removed
325 using a solution of 0.5 M hydroxylamine hydrochloride in 20% v/v acetic acid for 48h. Then, the organic matter
326 was removed with a 5% H_2O_2 solution for 48h.

327
328 The leached samples were dried and digested by alkaline fusion following the protocol of Bayon et al. (2009),
329 along with certified standards (BHVO-2, BRC-2) from the United States Geological Survey (USGS).
330 Approximately 50 mg of each sample underwent alkaline fusion in a carbon crucible with 0.6 g of NaOH and 1.2
331 g of Na_2O_2 heated at 650°C for 12 min in a furnace, before adding ultrapure water in which Fe-hydroxides
332 precipitated, concentrating rare earth elements. After centrifugation, the samples were dissolved in 3 ml 4 M HCl.

333
334 From this solution, an aliquot of 0.3 ml was extracted for analyses of Nd and Sm concentrations. Part of the
335 samples were measured for their Nd and Sm concentrations on an Agilent 7500 quadrupole ICP-MS spectrometer
336 in the Laboratoire Magmas et Volcans (LMV) in Clermont-Ferrand (France), and quantified using standard
337 bracketing with a solution of BHVO-2 during the session. Accuracy and reproducibility were assessed using two
338 BHVO-2 and one BCR-2 samples among the samples. Deviations of Nd and Sm concentrations from these
339 standards were below 11%. The other part of the samples was measured for their Nd and Sm concentrations on a
340 Thermo Scientific X-Series II® at the Pole Spectrométrie Océan in Brest (France), and quantified using multi-
341 element calibration standards prepared from single element standards purchased from SCP science (Baie d'Urfé,
342 Québec, Canada). Accuracy and reproducibility were assessed using one BHVO-2 and one BCR-2 sample, which
343 were analysed among the samples. Deviations of Nd and Sm concentrations from these standards were below 7%.

344
345 Purified neodymium fractions were isolated from the mother solution by ion chromatography following the
346 protocol described in Gaitan et al. (2023) for the low-pressure, automated column chromatography PrepFAST-
347 MC® system device, using AG50W-X8 (200-400 mesh) resin for rare earth element separation and Ln Spec (50-
348 100 μm) resin for Nd separation. Part of the neodymium isotopic measurements was performed on a MC-ICP-MS
349 Neptune Plus (Thermo Scientific) at the Laboratoire Magmas et Volcans in Clermont-Ferrand (France). Ratios
350 were corrected for mass bias using an exponential law and a $^{143}\text{Nd}/^{144}\text{Nd}$ ratio of 0.7219. Mass-bias-corrected
351 $^{143}\text{Nd}/^{144}\text{Nd}$ were normalised to a JNdi-1 value of 0.512115 (Tanaka et al., 2000). Repeated measurements of
352 JNdi-1 throughout the session gave an external reproducibility of ± 0.000009 (2σ , $n = 15$), corresponding to \pm
353 0.18 in the standard $\epsilon_{\text{Nd}}(0)$ notation. Analyses of two BHVO-2 reference materials yielded a $^{143}\text{Nd}/^{144}\text{Nd}$ ratio of
354 0.512991 ± 0.000005 for each, in excellent agreement with the published value of 0.512990 ± 0.000010 (Weis et al.,
355 2005). The other part of the samples was analysed on an MC-ICP-MS Neptune Plus (Thermo Scientific) at the
356 ENS of Lyon (France). Ratios were corrected for mass bias using an exponential law and a $^{143}\text{Nd}/^{144}\text{Nd}$ ratio of
357 0.7219. Mass-bias-corrected $^{143}\text{Nd}/^{144}\text{Nd}$ values were normalised to a JNdi-1 value of 0.512115 (Tanaka et al.,
358 2000). Repeated measurements of JNdi-1 throughout the session gave an external reproducibility of ± 0.000018
359 (2σ , $n = 16$), corresponding to ± 0.34 in the standard $\epsilon_{\text{Nd}}(0)$ notation. Analyses of four BHVO-2 reference materials
360 gave an average $^{143}\text{Nd}/^{144}\text{Nd}$ ratio of 0.512985 ± 0.000009 for each, in agreement with the published value of
361 0.512990 ± 0.000010 (Weis et al., 2006).

362
363 The data are reported in the standard epsilon notation $\epsilon_{\text{Nd}} = [((^{143}\text{Nd}/^{144}\text{Nd})_{\text{sample}} / (^{143}\text{Nd}/^{144}\text{Nd})_{\text{CHUR}}) - 1] * 10^4$,
364 corrected for the radioactive decay of ^{147}Sm to ^{143}Nd based on the Nd and Sm concentrations measured for each
365 sample ($^{147}\text{Sm}/^{144}\text{Nd} = \text{Sm}/\text{Nd} * 0.6049$), an age of 55.8 Ma, and the ^{147}Sm radioactive decay constant λ ($6.54 \times$
366 10^{-12} y^{-1} ; Lugmair & Marti, 1977). The CHUR (CHondritic Uniform Reservoir) $^{143}\text{Nd}/^{144}\text{Nd}$ ratio was also
367 corrected using a $^{147}\text{Sm}/^{144}\text{Nd}$ ratio of 0.1960 and a present-day value of 0.512630 (Bouvier et al., 2008).

368 4. Results

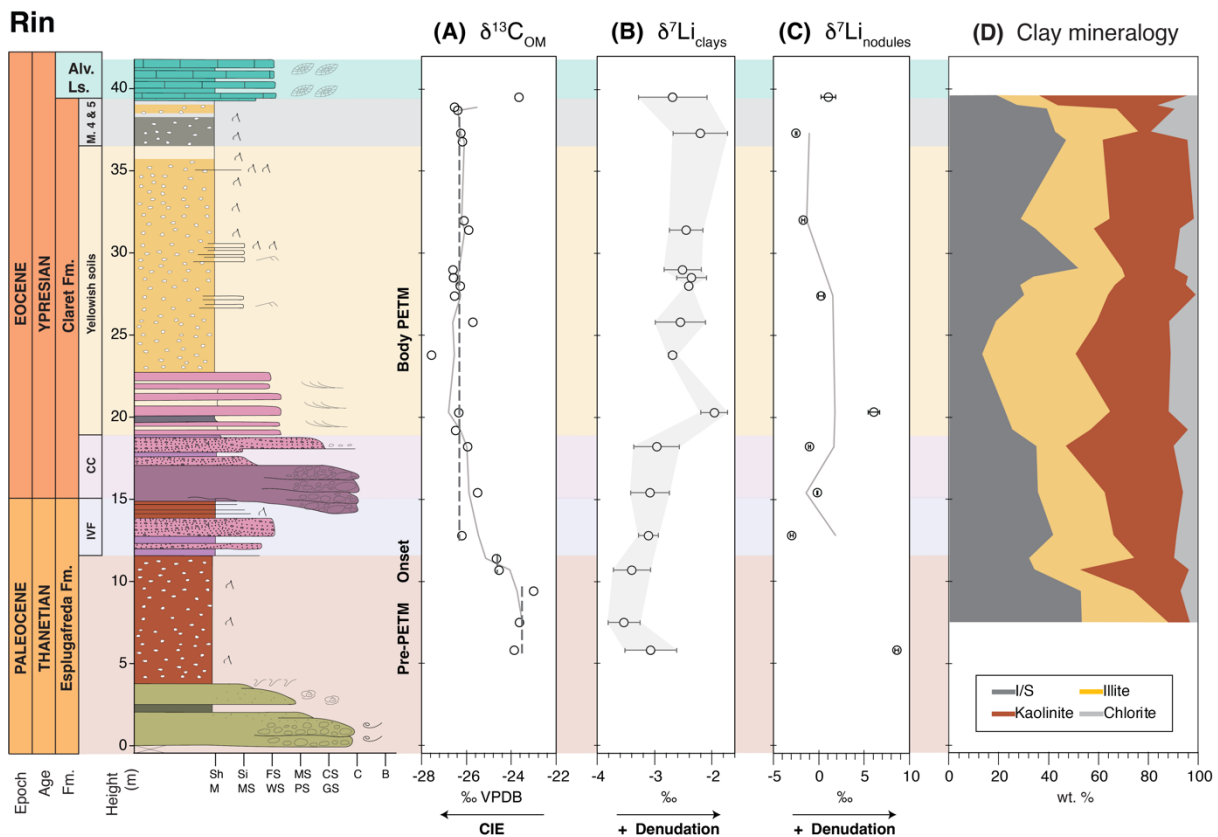
370 4.1. Clay mineralogy in the Rin section

371 The clay mineralogy in the Rin section (Fig. 5D, Table S1) comprises mixed-layer illite-smectite (I/S), with a
372 mean abundance of 34 ± 11 (1σ) wt.%; illite, 29 ± 9 wt.%; kaolinite, 30 ± 11 wt.%; and minor chlorite, 7 ± 5
373 wt.%. The pre-PETM samples have a mixed-layer I/S abundance of 42 ± 10 wt.%, decreasing to 32 ± 10 wt.%

374 during the body of the PETM. The kaolinite abundance increases from 22 ± 14 wt.% to 32 ± 9 wt.% during the
 375 PETM body, while the illite and chlorite abundances remain stable.

376 4.2. Organic matter carbon isotopes in the Rin section

377 Throughout the section, the mean $\delta^{13}\text{C}_{\text{OM}}$ value is -25.7‰ , with a standard deviation (1σ) of 1.2‰ (**Fig. 5A, Table**
 378 **S2**). The pre-PETM samples, between 5.8 and 9.4 m, have a mean value of $-23.5 \pm 0.5\text{‰}$. A negative excursion
 379 begins in samples at 10.7 and 11.4 m, with values decreasing to $-24.6 \pm 0.1\text{‰}$. The most depleted values occur
 380 between 12.8 and 38.9 m, with a mean of $-26.3 \pm 0.5\text{‰}$. The final sample at 39.5 m, below the Alveolina
 381 Limestone, suggests a return to pre-PETM levels, with a value of -23.7‰ .
 382



383 **Figure 5.** Rin section isotopes and clay mineralogy. (A) The $\delta^{13}\text{C}_{\text{OM}}$ record shows the negative Carbon Isotope
 384 Excursion (CIE), with an onset before the Claret Conglomerate and sustained negative values until the Alveolina
 385 Limestone. (B) The CIE was accompanied by a positive excursion in lithium isotopes of the clays ($\delta^7\text{Li}_{\text{clays}}$),
 386 reaching a 0.9‰ excursion in the Yellowish soils member. (C) Lithium isotopes in the carbonate nodules showed
 387 high variability and a less conclusive trend. (D) Rin section clay mineralogy. The pre-PETM and body intervals
 388 were determined based on the $\delta^{13}\text{C}_{\text{OM}}$ record and the stratigraphy. Dashed lines in panel A represent average
 389 values for $\delta^{13}\text{C}_{\text{OM}}$ in the pre-PETM and syn-PETM intervals. Grey bars in panel B outline the analytical
 390 uncertainty (2sd) of $\delta^7\text{Li}_{\text{clays}}$.
 391

392 4.3. Lithium isotopes in the Rin and Esplugafreda sections

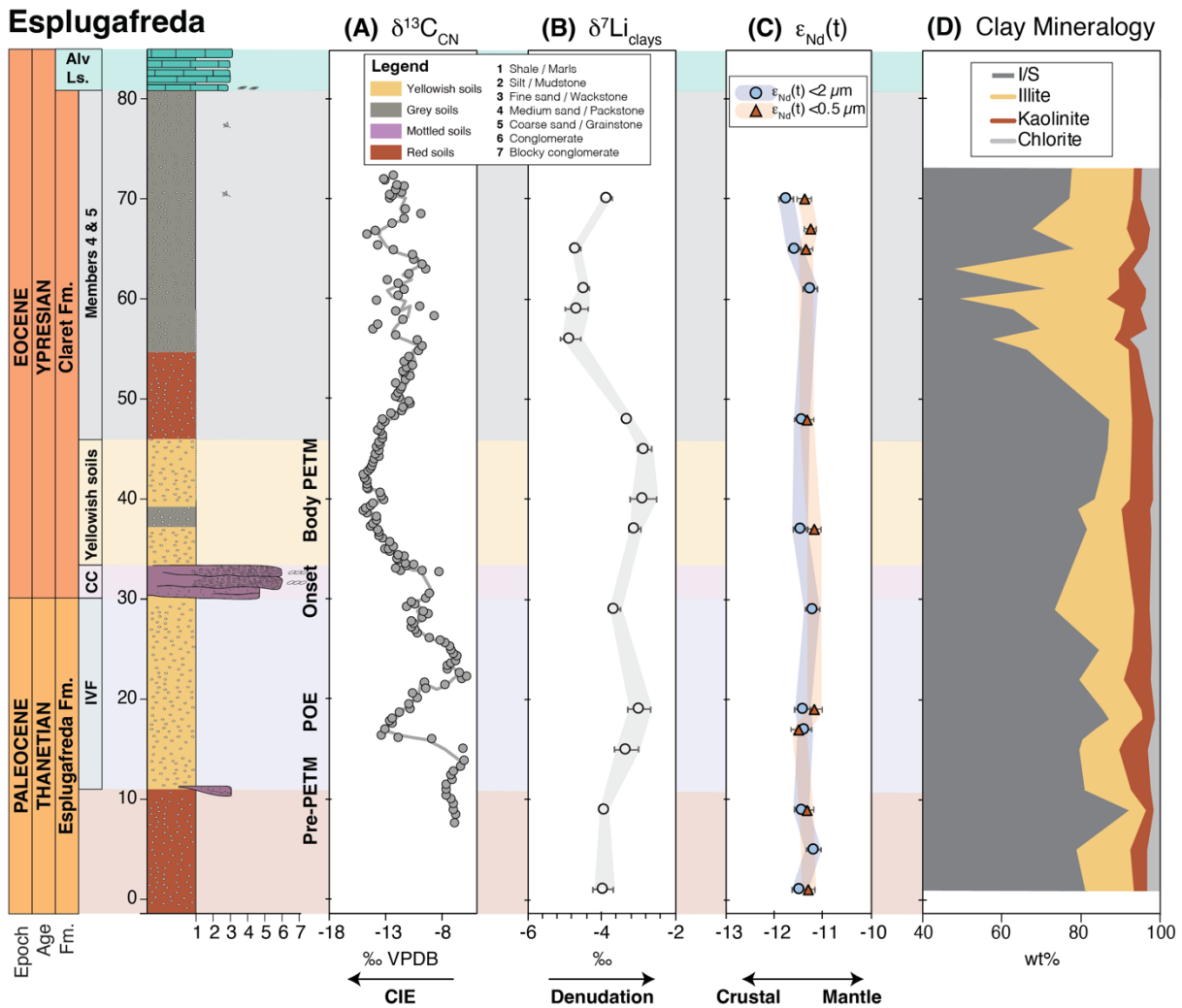
393 The clays of the Rin section have a mean lithium isotope composition of $-2.9 \pm 0.5\text{‰}$ (1σ) (**Fig. 5B, Table S2**).
 394 Between 5.8 and 18.2 m, the mean composition is $-3.4 \pm 0.2\text{‰}$. Above this, from 20.3 to 39.5 m, the mean
 395 composition is $-2.6 \pm 0.2\text{‰}$, which corresponds to a shift towards more positive values of $\sim 0.8\text{‰}$. The minimum
 396 value of -3.7‰ is seen before the Claret Conglomerate, and the maximum value of -2.2‰ occurs immediately
 397 after the Claret Conglomerate, indicating a total range of up to $\sim 1.5\text{‰}$. The $\delta^7\text{Li}$ values measured on carbonate
 398 nodules have a maximum value of 8.6‰ , a minimum value of -3.0‰ , and a mean composition of $0.9 \pm 4.0\text{‰}$
 399 (**Fig. 5C**). No clear temporal trend is observed in the $\delta^7\text{Li}_{\text{nodules}}$ record. No systematic correlation is observed
 400 between $\delta^7\text{Li}_{\text{clays}}$ and the relative abundance of individual clay minerals within analytical uncertainty (**Fig. S1**).
 401

402 At the Esplugafreda section, the clays have a mean lithium isotope composition of $-3.7 \pm 0.7\text{‰}$ (**Fig. 6B, Table**
 403 **S3**). The pre-PETM samples (0-10 m and 21-28 m, Jaimes-Gutierrez et al., 2024 and references therein) have a

404 mean composition of $-3.8 \pm 0.2\%$. The POE samples ($\sim 15\text{--}21\text{ m}$) have a composition of $-3.2 \pm 0.2\%$, and the
 405 syn-PETM sediments have a composition of $-3.0 \pm 0.2\%$, indicating a PETM shift towards more positive values
 406 of $\sim 0.8\%$. The post-PETM sediments have a composition of $-4.5 \pm 0.4\%$. Samples from the pre-PETM, Pre-
 407 Onset Excursion (POE), and syn-PETM intervals display relatively heavier $\delta^7\text{Li}_{\text{clays}}$ values, whereas recovery-
 408 phase samples form a distinct cluster characterised by lighter $\delta^7\text{Li}_{\text{clays}}$ (Fig. S2).
 409

4.4. Neodymium isotopes in the Esplugafreda sections

411 Throughout the Esplugafreda section, the $0.5\text{--}2\ \mu\text{m}$ clays have a mean $\epsilon_{\text{Nd}}(t = 55.8\text{ Ma})$ composition of $-10.94 \pm$
 412 $0.16 (2\sigma)$, while the $<0.5\ \mu\text{m}$ fraction has a mean composition of -10.88 ± 0.11 (Fig. 6C, Table S4). In comparison,
 413 the typical analytical uncertainty on any individual sample measurement was $0.21 (2\sigma)$. Hence, these values are
 414 considered constant through time, with no deviation significantly outside the analytical uncertainty. The
 415 neodymium isotope measurements on the $<0.5\ \mu\text{m}$ fraction are also indistinguishable from those on the $0.5\text{--}2\ \mu\text{m}$
 416 fraction (Fig. 6C).
 417



418 **Figure 6.** Esplugafreda section isotopes and clay mineralogy. (A) The $\delta^{13}\text{C}$ record from microcrystalline
 420 carbonate nodules (from Khozyem, 2013) shows a negative carbon isotope excursion during the Pre-Onset
 421 Excursion (POE) and during the main body of the PETM. (B) Positive excursions in lithium isotopes of the clays
 422 ($\delta^7\text{Li}_{\text{clays}}$) during both the POE and the main CIE of the PETM. (C) Neodymium isotopes ($\epsilon_{\text{Nd}}(t = 55.8\text{ Ma})$) show
 423 no variation throughout the section, indicating constant provenance. (D) Esplugafreda section clay mineralogy
 424 (modified from Jaimes-Gutierrez et al., 2024).

425 5. Discussion

426 5.1. The PETM in the Rin section

427 The PETM sediments in the Rin section represent an archive of the climatic perturbation in a coastal terrestrial
 428 setting (Pujalte et al., 2014; Prieur et al., 2025). This locality records a negative $\delta^{13}\text{C}_{\text{OM}}$ excursion of -2.8% from

429 pre- to syn-PETM (**Fig. 5**), in agreement with the CIE excursion of 3-5 ‰ identified in other southern Pyrenean
430 sections and other global settings (e.g. Schmitz et al., 2001; Schmitz and Pujalte, 2007; McInerney and Wing,
431 2011; Pujalte et al., 2015). The slightly reduced magnitude compared to the global record is consistent with
432 observed systematic differences in the CIE across different types of terrestrial archives, with paleosol carbonates
433 typically recording a 1-2 ‰ larger CIE than paleosol organic matter (Bowen et al., 2004; Cotton et al., 2015;
434 Gallagher et al., 2019). We do not identify the POE in the Rin section, and we suggest that it may have been
435 missed due to its occurrence further down in the section. Likewise, the recovery to pre-PETM values is also largely
436 absent, with just one sample below the Alevolina Limestone showing less depleted $\delta^{13}\text{C}_{\text{OM}}$ values.

437
438 The five members recognised in the Claret Fm. show an evolution from the eastern terrestrial setting into the
439 western marine domain. At Esplugafreda (**Fig. 6**), the five members are recorded (Basilici et al., 2022 and
440 references therein), including Member 1, IVF (pre-PETM); Member 2, the Claret Conglomerate (Onset at
441 Esplugafreda); Member 3, Yellowish soils (syn-PETM, or body of the PETM); Member 4, red paleosols with
442 gypsum; and Member 5, consisting of red mudstones with carbonate nodules (e.g. Schmitz and Pujalte, 2007;
443 Baceta et al., 2011; Pujalte et al., 2014; Colomera et al., 2017; Basilici et al., 2022). However, Member 4, the
444 gypsum-rich member, only occurs in the eastern part of the basin (Pujalte et al., 2014). Given the coastal position
445 of the Rin section, at the marine-continental transition and only ~20 km east of the Serraduy section, representing
446 the westernmost expression of the interfingering between continental deposits from the Esplugafreda Fm. and
447 marine carbonates (Prieur et al., 2025), the absence of Member 4 supports a further downstream position of the
448 Rin section relative to the Esplugafreda floodplain section.

449
450 Duller et al. (2019) estimated a lag time of approximately 16.5 ± 7.5 kyr between the CIE and the onset of coarse-
451 grained deposition at terrestrial sites in the Pyrenees. While sections such as Tendrui, Claret, and Campo (Pujalte
452 et al., 2009; Domingo et al., 2009) display a stratigraphic offset consistent with this lag, the Esplugafreda section
453 does not show such an offset (Duller et al., 2019). In the Rin section discussed here, we observe a clear offset
454 between the onset of the CIE and the arrival of the Claret Conglomerate (**Fig. 5**). To correctly position the lag
455 time and explore the missing POE, future work could focus on high-resolution $\delta^{13}\text{C}$ characterisation of the section.

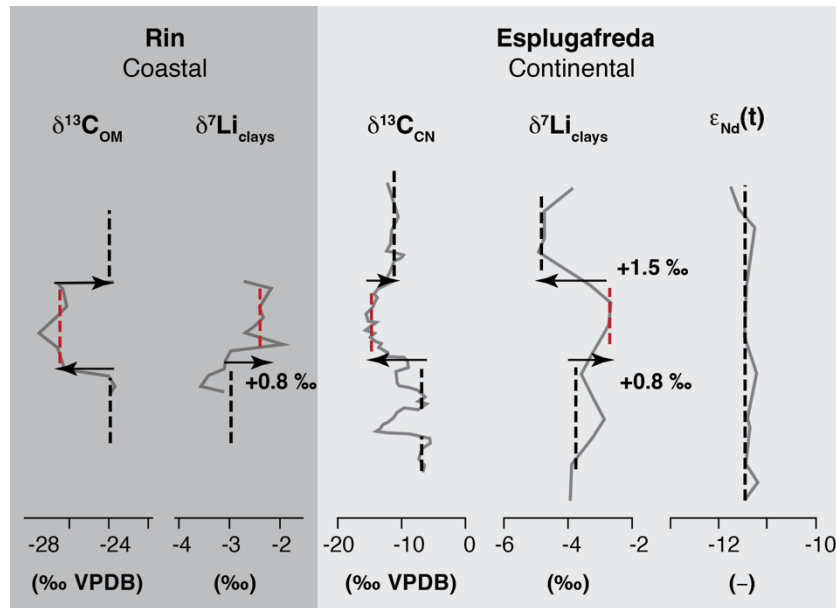
456
457 The clay mineralogy at Rin further suggests a potential signal propagation effect. A shift from smectite-dominated
458 clays during the pre-PETM interval to an increase in kaolinite during the syn-PETM interval (**Fig. 5D**) could
459 indicate a transition to more hydrolysing conditions and to an increase in weathering intensity, or enhanced erosion
460 of former sedimentary formations rich in kaolinite. However, this trend also corresponds to a downstream
461 transition from authigenic smectite-rich paleosols at Esplugafreda (**Fig. 6D**) (e.g. Khozyem, 2013; Basilici et al.,
462 2022; Jaimes-Gutierrez et al., 2024) to kaolinite-dominated sediments in the Zumaia deep-marine section
463 (Gawenda et al., 1999; Schmitz et al., 2001; Bolle and Adatte, 2001). This mineralogical gradient from
464 Esplugafreda to Rin and Zumaia underscores the system connectivity across the basin (Pujalte et al., 2014).
465 However, such variations in clay composition may also reflect differences in sediment provenance (although
466 temporal changes are not observed in the ϵ_{Nd} record from Esplugafreda); differential mineral transport; enhanced
467 floodplain weathering; an increased proportion of eroded sedimentary formations downstream, bringing reworked
468 kaolinite (Pujalte et al., 2015); or a larger catchment area feeding the marine system (Chamley, 1989 and
469 references therein).

470
471 An influence from Marine Authigenic Aluminosilicate Clay (MAAC) formation is feasible in the coastal setting
472 of the Rin section, but is unlikely to have been a significant driver of changes in the lithium isotope record given
473 the dominance of continental inputs. In marine sediments, clay mineral assemblages dominated by kaolinite, illite,
474 smectite, and mixed-layer illite/smectite are generally interpreted as mainly detrital in origin, reflecting
475 continental weathering and fluvial transport rather than in situ marine precipitation (Thiry, 2000; Fagel, 2007;
476 Velde and Meunier, 2008). Although the authigenic formation of these clay minerals is known to occur in marine
477 environments, it is typically restricted to specific conditions or processes, such as the alteration of volcanic ash,
478 or evaporitic or hydrothermal settings, and is therefore not expected to be significant in shallow, nearshore
479 depositional systems with high terrigenous sedimentation rates (Środoń, 2001; Wise et al., 2001; Meunier, 2005).
480 In contrast to glauconite or other green clays, which may form authigenically under low sedimentation rates,
481 kaolinite and illite in coastal marine settings are widely regarded as inherited from continental sources (Thiry,
482 2000; Meunier, 2005; Fagel, 2007; Presti and Michalopoulos, 2008; Bernhardt et al., 2020). Given the dominantly
483 continental depositional setting of the Rin section and the large detrital clay input inferred for the nearshore
484 environment, any MAAC contribution is expected to have been minor relative to the terrigenous signal. MAAC
485 form from isotopically heavy seawater or porewaters and are therefore expected to have $\delta^7\text{Li}$ values substantially
486 higher than detrital clays (Pogge von Strandmann et al., 2021a). A simple mass balance indicates that even under
487 extreme assumptions (i.e. 2 wt.% MAAC, 10‰ $\delta^7\text{Li}$ values), such a contribution would shift bulk values by
488 <0.3‰, far smaller than the observed PETM excursion.

489

490 **5.2. Evolution of weathering intensity in the continental realm of the Southern Pyrenees**

491 Our $\delta^7\text{Li}_{\text{clays}}$ records from Rin and Esplugafreda both show a positive ($\sim 1\%$) lithium isotope excursion in the
 492 continental Southern Pyrenees during the onset and body of the PETM (**Fig. 7**). The $\delta^7\text{Li}$ values from carbonate
 493 nodules at Rin show greater variability (**Fig. 5C**), but remain inconclusive due to potential clay contamination or
 494 cation exchange between clays and carbonates (e.g. Pogge von Strandmann et al., 2019). Given the high Li content
 495 in silicate minerals, even a minor clay particle content in the nodules could contaminate the carbonate signature.
 496 Critically, the invariant ϵ_{Nd} composition of both size fractions throughout the Esplugafreda record (**Fig. 6C**)
 497 supports a constant provenance of the sediments, which suggests that the $\delta^7\text{Li}_{\text{clays}}$ records can be reliably
 498 interpreted as a reflection of weathering regime changes in response to the climatic perturbation.
 499



500

501

502 **Figure 7.** Comparison of isotopic results from the Rin and Esplugafreda sections. Grey solid lines show the raw
 503 data, while dashed black and red lines indicate typical values for different intervals, where red represents the
 504 syn-PETM. The pre-PETM and post-PETM shifts are indicated with the black arrows, and the magnitudes of the
 505 $\delta^7\text{Li}_{\text{clays}}$ excursions are reported.
 506

507

508 In many other PETM records, both marine and terrestrial $\delta^7\text{Li}$ values show a negative excursion from pre-PETM
 509 to syn-PETM conditions. Pogge von Strandmann et al. (2021) documented a negative $\delta^7\text{Li}$ excursion of $\sim 3\%$
 510 during the PETM in several marine carbonate sections and in detrital shales, indicating intensified global erosion
 511 rates (by 2–3 \times) and a 50–60% increase in silicate weathering fluxes, which was proposed to have contributed to
 512 climate stabilisation. Ramos et al. (2022) also found a negative $\delta^7\text{Li}_{\text{clays}}$ excursion, albeit with a smaller magnitude
 513 of $\sim 1.5\%$, in fine sediments of the Bighorn Basin, North America, during the PETM, and this change was
 514 sustained during the recovery phase. Marine records off the North American margin also reflect a negative
 515 excursion in the Gulf of Mexico (0.4–1.5 $\%$) and the Mid-Atlantic Coast ($\sim 3\%$) (Jaimes-Gutierrez et al., 2025;
 516 Rush et al., 2025). Consistent with these results, Chen et al. (2023) found a negative $\delta^7\text{Li}_{\text{clays}}$ excursion of $\sim 3\%$
 517 in the Nanyang Basin, East Asia, which, together with the negative $\delta^7\text{Li}$ excursion in the lacustrine carbonates, was
 518 interpreted as recording a doubling of the regional silicate weathering intensity during the PETM.

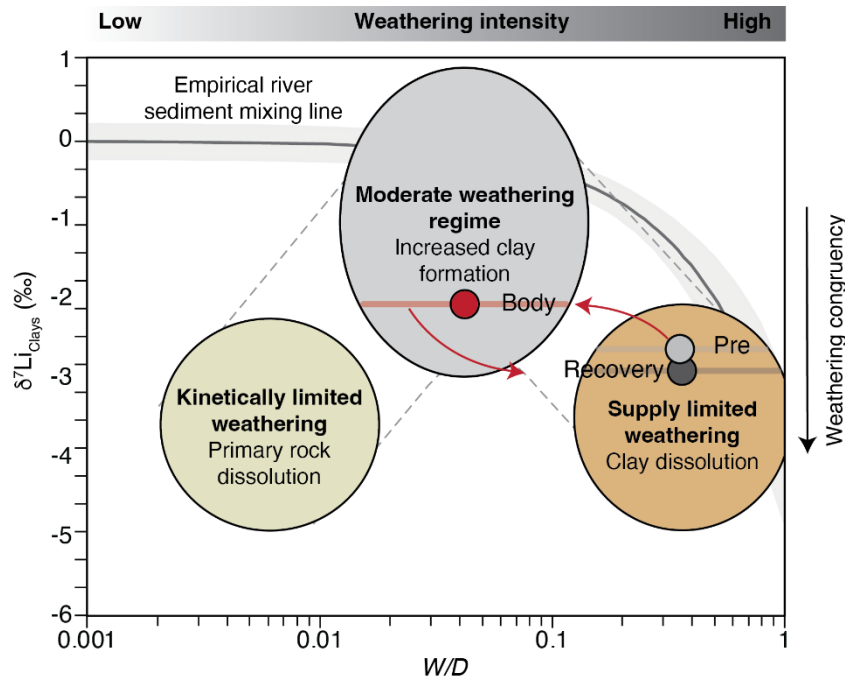
519

520 Why, then, do the Southern Pyrenees floodplains record a positive $\delta^7\text{Li}_{\text{clays}}$ excursion during the PETM? We
 521 interpret the positive $\delta^7\text{Li}_{\text{clays}}$ excursion during the PETM as a shift towards increased incongruent weathering
 522 (moderate weathering regime), characterised by enhanced clay formation in the floodplain deposits. This regime
 523 would be characterised by increased chemical weathering, but relatively greater increases in physical erosion and
 524 sediment transport (e.g. Pujalte et al., 2015; Chen et al., 2018; Prieur et al., 2024), due to enhanced runoff causing
 525 short water residence times and rapid sediment export (i.e. lower W/D ; **Fig. 8**). Hydrological changes during the
 526 PETM are widely documented in the Southern Pyrenees (Schmitz and Pujalte, 2007; Pujalte et al., 2015; Chen et
 527 al., 2018; Rush et al., 2021; Prieur et al., 2024, 2025; Jaimes-Gutierrez et al., 2024) and likely played a central
 role in driving those weathering changes. A shift towards more intense, episodic rainfall, without an increase in

528 mean annual precipitation (Rush et al., 2021), could have reduced infiltration, increased runoff, and shortened
 529 water–mineral interaction times. These processes would lead to decreased clay formation in the uplands by
 530 shortening water–rock interaction times (Kump et al., 2000; Riebe et al., 2004), while shifting clay production and
 531 accumulation towards lowland environments, where longer sediment residence times promote authigenic clay
 532 formation, consistent with modern river floodplain processes (e.g. Dellinger et al., 2015; Maffre et al., 2020). We
 533 also note that weathering processes are highly heterogeneous, and therefore global variability during the PETM
 534 can be expected (e.g. Frings, 2019). Critically, A decrease in W/D can lead both to positive or negative $\delta^7\text{Li}$
 535 excursions, depending on the starting weathering regime (Krause et al., 2023).

537 Increasing evaporation, as recorded by gypsum lenses in Esplugafreda (Baceta et al., 2011; Khozyem, 2013;
 538 Jaimes-Gutierrez et al., 2024 and references therein), could also result in oversaturated pore waters, favouring
 539 clay formation. Experimental and field-based studies show that enhanced evaporation and reduced water
 540 availability increase the dissolved $\delta^7\text{Li}$ values in soil and pore waters, leading to higher $\delta^7\text{Li}$ compositions of clays
 541 forming in equilibrium with these fluids (Xu et al., 2022; Pogge von Strandmann et al., 2023). Hydrological
 542 controls can also influence the $\delta^7\text{Li}_{\text{clays}}$ signatures by regulating water–rock interactions, sediment transport, and
 543 secondary mineral formation (Fig. 8). In supply-limited weathering regimes, increased runoff shortens water–
 544 rock interaction times and lowers dissolved $\delta^7\text{Li}$ values in river waters (Zhang et al., 2022), while enhanced
 545 sediment transfer promotes sediment storage and prolonged water–sediment interaction in floodplains, where
 546 continued clay alteration and isotopic re-equilibration can yield relatively higher $\delta^7\text{Li}$ values in the clay fraction
 547 preserved in lowland deposits. Overall, rapid sediment transport limits basin-scale weathering intensity, despite
 548 localised clay formation in floodplain environments.

549



550

551 **Figure 8.** Weathering regime change from pre-PETM to syn-PETM based on $\delta^7\text{Li}_{\text{clays}}$ in the continental deposits
 552 of the Southern Pyrenees. The floodplain records were characterised by a decrease in weathering intensity and
 553 an increase in clay formation. Enhanced transport efficiency resulted in a major increase in physical erosion,
 554 with reaction kinetics limiting chemical weathering. Modified from Dellinger et al. (2015, 2017). At low W/D , the
 555 empirical river sediment mixing line includes the effects of mixing with primary minerals.

556 In the Esplugafreda section, the Recovery phase sees a shift towards more negative values than the pre-PETM
 557 conditions. During this interval, we observe a coeval increase in illite, kaolinite, and chlorite abundances in the
 558 Esplugafreda section (Jaimes-Gutierrez et al., 2024). This shift in the clay mineral assemblage strongly suggests
 559 an increase in detrital input. For this reason, we consider that the observed excursion cannot be straightforwardly
 560 interpreted as a change in weathering intensity, but rather reflect the clay mineral assemblage (Fig. S2).

561

562 Temperature effects on lithium isotope fractionation are minor in the Southern Pyrenees. While lithium isotope
 563 fractionation during clay formation is temperature-dependent (Vigier et al., 2008; Li and West, 2014), the
 564 fractionation factor (α) for incorporation in smectite is nearly constant across typical surface weathering
 565 temperatures (Vigier et al., 2008). Using the ~ 3 °C warming estimated for the continental Pyrenees across the

566 PETM (Jaimes-Gutierrez et al., 2024), the maximum temperature-driven change in clay $\delta^7\text{Li}$ values is expected
567 to be only a few tenths of a per mil (Li and West, 2014). This effect would shift clay $\delta^7\text{Li}$ values slightly towards
568 heavier values and could therefore contribute marginally to the observed excursion, but it is insufficient to explain
569 the full magnitude of the $\sim 1\text{‰}$ positive $\delta^7\text{Li}_{\text{clays}}$ shift observed in the records. Hence, climatic and hydrological
570 processes, rather than direct temperature effects, must dominate the $\delta^7\text{Li}$ signal.
571

572 The differences in $\delta^7\text{Li}$ values between river water and bedrock are controlled by the balance between lithium
573 release by mineral dissolution and lithium removal by secondary mineral formation (Bouchez et al., 2013). The
574 Southern Pyrenees during the PETM was a relatively high-erosion regime, such that physical erosion dominated,
575 increasing the sediment supply and exposing fresh minerals (Schmitz and Pujalte, 2007; Pujalte et al., 2015, 2016;
576 Chen et al., 2018; Prieur et al., 2024, 2025). When erosion exposes fresh minerals, weathering rates increase with
577 total denudation, albeit less strongly than the increases in erosion, consistent with shared controls on chemical
578 weathering and physical denudation rates (Riebe et al., 2004; West et al., 2005). Even though high-relief regions
579 produce weakly weathered sediments, their high sediment yields and moderate clay formation rates result in
580 elevated weathering fluxes (Gaillardet et al., 1999). Therefore, we propose that the Southern Pyrenean floodplains
581 record a shift from a high-weathering intensity regime to a moderate-weathering intensity regime during the
582 PETM (Fig. 8). The pre-PETM conditions were characterised by a low reactivity of the parent lithology (Kump
583 and Arthur, 1997; Caves Rugenstein et al., 2019), associated with the carbonate-rich, reworked sediments in the
584 floodplain deposits, and hence low total weathering fluxes. The above scenario is also consistent with the "system-
585 clearing" event documented in western North America (Foreman et al., 2012), where sediment transport surged
586 in response to rapid climatic forcing, as well as with other Eocene warming events such as the Mid-Eocene
587 Climatic Optimum, which saw a shift towards enhanced clay formation and a lower weathering intensity (Krause
588 et al., 2023).
589

590 The progressive increase in kaolinite content from Esplugafreda to Rin may reflect an evolving weathering signal
591 during sediment transport from the hinterland towards the coastal plains, which potentially extended into the
592 marine realm. This scenario supports a basin-wide connectivity between climate-driven terrestrial processes and
593 marine sedimentary records. In addition, the increase in kaolinite content from Esplugafreda to Rin supports a
594 shift in clay formation processes during the PETM. Kaolinite is typically associated with intense leaching and
595 more advanced weathering, often forming under warm, humid, and periodically saturated conditions (Chamley,
596 1989; Velde and Meunier, 2008). Hence, its enrichment suggests either intensified in-situ clay formation in the
597 floodplains or increased transport of weathered material from the uplands to the lowlands. In either case, this shift
598 implies greater clay mineral production, consistent with a more incongruent weathering regime driving the
599 observed positive $\delta^7\text{Li}_{\text{clays}}$ excursion. Alternatively, enhanced kaolinite supply from the erosion-driven
600 exhumation of older sediments cannot be ruled out based on the current evidence.
601

602 Despite these insights, key questions remain unresolved. In particular, a comprehensive study of the provenance
603 and evolution of clay mineralogy is still needed to determine to what extent the observed patterns along the
604 sediment routing system reflect changes in weathering intensity, differential mineral transport, or sediment
605 reworking. Equally important is the need to constrain the precise age of the clay formation in relation to the timing
606 of the different phases of the PETM, which is critical for reconstructing the temporal dynamics of the weathering
607 regime in the Southern Pyrenees. Addressing these gaps will be crucial for better understanding how continental
608 weathering systems responded to extreme climatic perturbations in the past and how they may behave under future
609 global warming scenarios.
610

611 6. Conclusions

612 We explored the silicate weathering response to the PETM in two terrestrial sections from the Tremp-Graus Basin
613 of the Southern Pyrenees. These floodplain records show a positive $\delta^7\text{Li}_{\text{clays}}$ excursion, contrasting with the
614 commonly observed global negative $\delta^7\text{Li}$ excursion in clays and carbonates. We interpret this excursion as
615 reflecting a shift towards a moderate-intensity, incongruent weathering regime from an initial high-intensity,
616 supply-limited regime. The high erosion rates associated with increased extreme rainfall events and channel
617 mobility may have been the central factor influencing sediment residence times, with rapid sediment transport
618 limiting the extent of chemical weathering. Nevertheless, the elevated denudation rates would have led to higher
619 sediment and dissolved cation fluxes to the ocean, thereby enhancing regional CO_2 drawdown.
620

621 We explored two potential archives for recording continental weathering processes using lithium isotopes. The
622 clay records show a distinct response, reflected in positive $\delta^7\text{Li}_{\text{clays}}$ excursions synchronous with the negative CIE.
623 However, the $\delta^7\text{Li}_{\text{nodules}}$ signal recorded in the carbonate nodules is less conclusive, and we interpret the high

624 temporal variability as a sign of potential contamination by clays in the nodules. Given that Li concentrations in
625 silicate minerals are higher than in carbonates by several orders of magnitude, even minor amounts of clays could
626 have resulted in a mixed response in the nodules. Future studies should explore weaker leaching approaches on
627 such nodules and seek to validate such data with major and trace element analyses.

628
629 Provided coeval formation, the increase in kaolinite content from Esplugafreda to Rin provides mineralogical
630 support for more hydrolysing conditions and clay formation during the PETM in the Tremp-Graus Basin,
631 reinforcing the interpretation of more incongruent weathering under altered hydroclimatic conditions. Notably,
632 the parent material in these floodplain paleosols is carbonate-rich and relatively unreactive. These results highlight
633 the critical role of hydrological controls, especially rainfall intensity, runoff dynamics, and sediment residence
634 time, in shaping continental weathering responses during extreme climate events.

635
636 Finally, we propose that to fully quantify weathering dynamics during the PETM in the Southern Pyrenees, further
637 work is needed to: (1) constrain the chronology of clay formation; (2) trace the evolution of clay mineralogy and
638 provenance from source to sink; and (3) integrate continental and marine weathering records across the sediment
639 routing system. Together, these steps will be essential for refining our understanding of weathering behaviour and
640 the associated climate feedbacks under rapid climatic perturbations, and for improving predictions of Earth's
641 surface processes in semi-arid floodplain systems in future global warming scenarios.

642

643 **Acknowledgments**

644 We acknowledge funding from the European Union's Horizon 2020 research and innovation programme under
645 the Marie Skłodowska-Curie grant agreement No. 860383 S2S FUTURE. D.J.W. was supported by a NERC
646 independent research fellowship (NE/T011440/1). We thank Justine Blondet for her support in neodymium
647 isotope chromatography. We thank Dr. Gaojun Li and an anonymous reviewer for their constructive comments
648 that helped improve the manuscript.

649

650 **Author contributions**

651 R.J.G. performed sample collection, analytical work (clay mineralogy, RockEval, lithium and neodymium ion-
652 exchange chromatography), data interpretation, visualisation, and original manuscript writing.

653 M.P. contributed to sample collection, data interpretation, visualisation, and manuscript writing.

654 D.J.W. and P.A.E.P.V.S. contributed to analytical work on lithium isotopes, data interpretation, and manuscript
655 writing.

656 E.P. conducted analytical work on neodymium isotopes, data interpretation, and manuscript writing.

657 T.A. conducted RockEval analyses, contributed to data interpretation, and manuscript writing.

658 J.E.S. conducted $\delta^{13}\text{C}$ analyses on organic matter and contributed to data interpretation and manuscript writing.

659 S.C. acquired funding for the project, contributed to sample collection, data interpretation, and manuscript writing.

660

661 **Conflict of interest**

662 The authors declare that they have no conflict of interest relevant to this study.

663

664 **References**

665 Adatte, T., Stinnesbeck, W., and Keller, G., 1996, Lithostratigraphic and mineralogic correlations of near K/T
666 boundary clastic sediments in northeastern Mexico: Implications for origin and nature of deposition, *in*
667 The Cretaceous-Tertiary Event and Other Catastrophes in Earth History, Geological Society of
668 America, doi:10.1130/0-8137-2307-8.211.

669 Anderson, S.P., Von Blanckenburg, F., and White, A.F., 2007, Physical and Chemical Controls on the Critical
670 Zone: Elements, v. 3, p. 315–319, doi:10.2113/gselements.3.5.315.

671 Baceta, J.I., Pujalte, V., and Bernaola, G., 2005, Paleocene corallgal reefs of the western Pyrenean basin,
672 northern Spain: New evidence supporting an earliest Paleogene recovery of reefal ecosystems:
673 Palaeogeography, Palaeoclimatology, Palaeoecology, v. 224, p. 117–143,
674 doi:10.1016/j.palaeo.2005.03.033.

675 Baceta, J.I., Pujalte, V., Wright, V.P., and Schmitz, B., 2011, Carbonate platform models, sea/ level changes and
676 extreme climatic events during the Paleocene/ Eocene greenhouse interval: A basin-platform-coastal
677 plain transect across the southern Pyrenean basin: 28th IAS Meeting of Sedimentology.

- 678 Barefoot, E.A., Nittrouer, J.A., Foreman, B.Z., Hajek, E.A., Dickens, G.R., Baisden, T., and Toms, L., 2022,
679 Evidence for enhanced fluvial channel mobility and fine sediment export due to precipitation
680 seasonality during the Paleocene-Eocene thermal maximum: v. 50, p. 116–120, doi:10.1130/G49149.1.
- 681 Basilici, G., Colombera, L., Soares, M.V.T., Arévalo, O.J., Mountney, N.P., Lorenzoni, P., de Souza Filho,
682 C.R., Mesquita, Á.F., and Janočko, J., 2022, Variations from dry to aquic conditions in Vertisols
683 (Esplugafreda Formation, Eastern Pyrenees, Spain): Implications for late Paleocene climate change:
684 Palaeogeography, Palaeoclimatology, Palaeoecology, v. 595, p. 110972,
685 doi:10.1016/j.palaeo.2022.110972.
- 686 Bauer, K.K., Vennemann, T.W., and Gilg, H.A., 2016, Stable isotope composition of bentonites from the Swiss
687 and Bavarian Freshwater Molasse as a proxy for paleoprecipitation: Palaeogeography,
688 Palaeoclimatology, Palaeoecology, v. 455, p. 53–64, doi:10.1016/j.palaeo.2016.02.002.
- 689 Bayon, G., Burton, K.W., Soulet, G., Vigier, N., Dennielou, B., Etoubleau, J., Ponzevera, E., German, C.R., and
690 Nesbitt, R.W., 2009, Hf and Nd isotopes in marine sediments: Constraints on global silicate
691 weathering: Earth and Planetary Science Letters, v. 277, p. 318–326, doi:10.1016/j.epsl.2008.10.028.
- 692 Bayon, G., German, C.R., Boella, R.M., Milton, J.A., Taylor, R.N., and Nesbitt, R.W., 2002, An improved
693 method for extracting marine sediment fractions and its application to Sr and Nd isotopic analysis:
694 Chemical Geology, v. 187, p. 179–199, doi:10.1016/S0009-2541(01)00416-8.
- 695 Behar, F., Beaumont, V., and De B. Penteadó, H.L., 2001, Rock-Eval 6 Technology: Performances and
696 Developments: Oil & Gas Science and Technology, v. 56, p. 111–134, doi:10.2516/ogst:2001013.
- 697 Bernhardt, A., Oelze, M., Bouchez, J., Von Blanckenburg, F., Mohtadi, M., Christl, M., and Wittmann, H.,
698 2020, ¹⁰Be/⁹Be Ratios Reveal Marine Authigenic Clay Formation: Geophysical Research Letters, v.
699 47, p. e2019GL086061, doi:10.1029/2019GL086061.
- 700 Bolle, M.-P., and Adatte, T., 2001, Palaeocene- early Eocene climatic evolution in the Tethyan realm: clay
701 mineral evidence: Clay Minerals, v. 36, p. 249–261, doi:10.1180/000985501750177979.
- 702 Bouchez, J., Von Blanckenburg, F., and Schuessler, J.A., 2013, Modeling novel stable isotope ratios in the
703 weathering zone: American Journal of Science, v. 313, p. 267–308, doi:10.2475/04.2013.01.
- 704 Bouvier, A., Vervoort, J.D., and Patchett, P.J., 2008, The Lu–Hf and Sm–Nd isotopic composition of CHUR:
705 Constraints from unequilibrated chondrites and implications for the bulk composition of terrestrial
706 planets: Earth and Planetary Science Letters, v. 273, p. 48–57, doi:10.1016/j.epsl.2008.06.010.
- 707 Bowen, G.J., Beerling, D.J., Koch, P.L., Zachos, J.C., and Quattlebaum, T., 2004, A humid climate state during
708 the Palaeocene/Eocene thermal maximum: Nature, v. 432, p. 495–499, doi:10.1038/nature03115.
- 709 Bufe, A., Hovius, N., Emberson, R., Rugenstein, J.K.C., Galy, A., Hassenruck-Gudipati, H.J., and Chang, J.-M.,
710 2021, Co-variation of silicate, carbonate and sulfide weathering drives CO₂ release with erosion:
711 Nature Geoscience, v. 14, p. 211–216, doi:10.1038/s41561-021-00714-3.
- 712 Carmichael, M.J. et al., 2017, Hydrological and associated biogeochemical consequences of rapid global
713 warming during the Paleocene-Eocene Thermal Maximum: Global and Planetary Change, v. 157, p.
714 114–138, doi:10.1016/j.gloplacha.2017.07.014.
- 715 Caves, J.K., Jost, A.B., Lau, K.V., and Maher, K., 2016, Cenozoic carbon cycle imbalances and a variable
716 weathering feedback: Earth and Planetary Science Letters, v. 450, p. 152–163,
717 doi:10.1016/j.epsl.2016.06.035.
- 718 Caves Rugenstein, J.K., Ibarra, D.E., and von Blanckenburg, F., 2019, Neogene cooling driven by land surface
719 reactivity rather than increased weathering fluxes: Nature, v. 571, p. 99–102, doi:10.1038/s41586-019-
720 1332-y.
- 721 Chamley, H., 1989, Clay Sedimentology: Berlin, Heidelberg, Springer Berlin Heidelberg, doi:10.1007/978-3-
722 642-85916-8.

- 723 Chen, Z., Ding, Z., Yang, S., Sun, J., Zhu, M., Xiao, Y., Tong, F., and Liang, Y., 2023, Strong Coupling
724 Between Carbon Cycle, Climate, and Weathering During the Paleocene-Eocene Thermal Maximum:
725 *Geophysical Research Letters*, v. 50, p. e2023GL102897, doi:10.1029/2023GL102897.
- 726 Chen, C., Guerit, L., Foreman, B.Z., Hassenruck-Gudipati, H.J., Adatte, T., Honegger, L., Perret, M., Sluijs, A.,
727 and Castellort, S., 2018, Estimating regional flood discharge during Palaeocene-Eocene global
728 warming: *Scientific Reports*, v. 8, p. 13391, doi:10.1038/s41598-018-31076-3.
- 729 Colombera, L., Arévalo, O.J., and Mountney, N.P., 2017, Fluvial-system response to climate change: The
730 Paleocene-Eocene Tresp Group, Pyrenees, Spain: *Global and Planetary Change*, v. 157, p. 1–17,
731 doi:10.1016/j.gloplacha.2017.08.011.
- 732 Cotton, J.M., Sheldon, N.D., Hren, M.T., and Gallagher, T.M., 2015, Positive feedback drives carbon release
733 from soils to atmosphere during Paleocene/Eocene warming: *American Journal of Science*, v. 315, p.
734 337–361, doi:10.2475/04.2015.03.
- 735 Dellinger, M., Bouchez, J., Gaillardet, J., Faure, L., and Moureau, J., 2017, Tracing weathering regimes using
736 the lithium isotope composition of detrital sediments: *Geology*, v. 45, p. 411–414,
737 doi:10.1130/G38671.1.
- 738 Dellinger, M., Gaillardet, J., Bouchez, J., Calmels, D., Louvat, P., Dosseto, A., Gorge, C., Alanoca, L., and
739 Maurice, L., 2015, Riverine Li isotope fractionation in the Amazon River basin controlled by the
740 weathering regimes: *Geochimica et Cosmochimica Acta*, v. 164, p. 71–93,
741 doi:10.1016/j.gca.2015.04.042.
- 742 Dessert, C., Dupré, B., Gaillardet, J., François, L.M., and Allègre, C.J., 2003, Basalt weathering laws and the
743 impact of basalt weathering on the global carbon cycle: *Chemical Geology*, v. 202, p. 257–273,
744 doi:10.1016/j.chemgeo.2002.10.001.
- 745 Dickens, G.R., O’Neil, J.R., Rea, D.K., and Owen, R.M., 1995, Dissociation of oceanic methane hydrate as a
746 cause of the carbon isotope excursion at the end of the Paleocene: *Paleoceanography*, v. 10, p. 965–
747 971, doi:10.1029/95PA02087.
- 748 Domingo, L., López-Martínez, N., Leng, M.J., and Grimes, S.T., 2009, The Paleocene–Eocene Thermal
749 Maximum record in the organic matter of the Claret and Tendrúy continental sections (South-central
750 Pyrenees, Lleida, Spain): *Earth and Planetary Science Letters*, v. 281, p. 226–237,
751 doi:10.1016/j.epsl.2009.02.025.
- 752 Dreyer, T., 1993, Quantified Fluvial Architecture in Ephemeral Stream Deposits of the Esplugafreda Formation
753 (Palaeocene), Tresp-Graus Basin, Northern Spain, *in* Marzo, M. and Puigdefàbregas, C. eds., *Alluvial*
754 *Sedimentation*, Wiley, p. 337–362, doi:10.1002/9781444303995.ch23.
- 755 Duller, R.A., Armitage, J.J., Manners, H.R., Grimes, S., and Jones, T.D., 2019, Delayed sedimentary response
756 to abrupt climate change at the Paleocene-Eocene boundary, northern Spain: *Geology*, v. 47, p. 159–
757 162, doi:10.1130/G45631.1.
- 758 Eichenseer, H., 1988, *Facies Geology Of Late Maestrichtian To Early Eocene Coastal And Shallow Marine*
759 *Sediments (Tresp-Graus Basin, Northeastern Spain)*:
- 760 Eichenseer, H., and Luterbacher, H., 1992, The marine paleogene of the tresp region (NE Spain)-depositional
761 sequences, facies history, biostratigraphy and controlling factors: *Facies*, v. 27, p. 119–151,
762 doi:10.1007/BF02536808.
- 763 Espitalie, J., Deroo, G., and Marquis, F., 1985, La pyrolyse Rock-Eval et ses applications. Deuxième partie.:
764 *Revue de l’Institut Français du Pétrole*, v. 40, p. 755–784, doi:10.2516/ogst:1985045.
- 765 Fagel, N., 2007, Chapter Four Clay Minerals, Deep Circulation and Climate, *in* *Developments in Marine*
766 *Geology*, Elsevier, v. 1, p. 139–184, doi:10.1016/S1572-5480(07)01009-3.

- 767 Foreman, B.Z., Heller, P.L., and Clementz, M.T., 2012, Fluvial response to abrupt global warming at the
768 Palaeocene/Eocene boundary: *Nature*, v. 491, p. 92–95, doi:10.1038/nature11513.
- 769 Frings, P.J., 2019, Palaeoweathering: How Do Weathering Rates Vary with Climate? *Elements*, v. 15, p. 259–
770 265, doi:10.2138/gselements.15.4.259.
- 771 Gaillardet, J., Dupré, B., and Allègre, C.J., 1999, Geochemistry of large river suspended sediments: silicate
772 weathering or recycling tracer? *Geochimica et Cosmochimica Acta*, v. 63, p. 4037–4051,
773 doi:10.1016/S0016-7037(99)00307-5.
- 774 Gaitan, C.E., Pucéat, E., Pellenard, P., Blondet, J., Bayon, G., Adatte, T., Israel, C., Robin, C., and Guillocheau,
775 F., 2023, Late Cretaceous erosion and chemical weathering record in the offshore Cape Basin: Source-
776 to-sink system from Hf Nd isotopes and clay mineralogy: *Marine Geology*, v. 466, p. 107187,
777 doi:10.1016/j.margeo.2023.107187.
- 778 Gallagher, T.M., Cacciatore, C.G., and Breecker, D.O., 2019, Interpreting the Difference in Magnitudes of
779 PETM Carbon Isotope Excursions in Paleosol Carbonate and Organic Matter: Oxidation of Methane in
780 Soils Versus Elevated Soil Respiration Rates: *Paleoceanography and Paleoclimatology*, v. 34, p. 2113–
781 2128, doi:10.1029/2019PA003596.
- 782 Gawenda, P., Winkler, W., Schmitz, B., and Adatte, T., 1999, Climate and bioproductivity control on carbonate
783 turbidite sedimentation (Paleocene to earliest Eocene, Gulf of Biscay, Zumaia, Spain): *Journal of*
784 *Sedimentary Research*, v. 69, p. 1253–1261, doi:10.2110/jsr.69.1253.
- 785 Gibbs, 1977, Clay Mineral Segregation in the Marine Environment: *SEPM Journal of Sedimentary Research*, v.
786 Vol. 47, doi:10.1306/212F713A-2B24-11D7-8648000102C1865D.
- 787 Goddérés, Y., Donnadiou, Y., Tombozafy, M., and Dessert, C., 2008, Shield effect on continental weathering:
788 Implication for climatic evolution of the Earth at the geological timescale: *Geoderma*, v. 145, p. 439–
789 448, doi:10.1016/j.geoderma.2008.01.020.
- 790 Gómez-Gras, D., Roigé, M., Fondevilla, V., Oms, O., Boya, S., and Remacha, E., 2016, Provenance constraints
791 on the Tremp Formation paleogeography (southern Pyrenees): Ebro Massif VS Pyrenees sources:
792 *Cretaceous Research*, v. 57, p. 414–427, doi:10.1016/j.cretres.2015.09.010.
- 793 Gutjahr, M., Frank, M., Stirling, C.H., Klemm, V., Van De Fliert, T., and Halliday, A.N., 2007, Reliable
794 extraction of a deepwater trace metal isotope signal from Fe–Mn oxyhydroxide coatings of marine
795 sediments: *Chemical Geology*, v. 242, p. 351–370, doi:10.1016/j.chemgeo.2007.03.021.
- 796 Hessler, A.M., Zhang, J., Covault, J., and Ambrose, W., 2017, Continental weathering coupled to Paleogene
797 climate changes in North America: *Geology*, v. 45, p. 911–914, doi:10.1130/G39245.1.
- 798 Hilton, R.G., 2023, Earth’s persistent thermostat: *Science*, v. 379, p. 329–330, doi:10.1126/science.adf3379.
- 799 Jaimes-Gutierrez, R., Adatte, T., Pucéat, E., Vennemann, T., Prieur, M., Wild, A.L., Khozyem, H., Vaucher, R.,
800 and Castelltort, S., 2024, Deciphering Paleocene-Eocene Thermal Maximum Climatic Dynamics:
801 Insights From Oxygen and Hydrogen Isotopes in Clay Minerals of Paleosols From the Southern
802 Pyrenees: *Paleoceanography and Paleoclimatology*, v. 39, p. e2024PA004858,
803 doi:10.1029/2024PA004858.
- 804 Jaimes-Gutierrez, R., Vimpere, L., Wilson, D.J., Blaser, P., Adatte, T., Sahoo, S., and Castelltort, S., 2025,
805 Lithium isotopes reveal enhanced weathering fluxes in North America during the Paleocene–Eocene
806 Thermal Maximum: *Geology*, doi:https://doi.org/10.1130/G53708.1.
- 807 Jones, M.T. et al., 2023, Tracing North Atlantic volcanism and seaway connectivity across the Paleocene–
808 Eocene Thermal Maximum (PETM): *Climate of the Past*, v. 19, p. 1623–1652, doi:10.5194/cp-19-
809 1623-2023.
- 810 Kennett, J.P., and Stott, L.D., 1991, Abrupt deep-sea warming, palaeoceanographic changes and benthic
811 extinctions at the end of the Palaeocene: *Nature*, v. 353, p. 225–229, doi:10.1038/353225a0.

- 812 Khozyem, H.M.A., 2013, Sedimentology, geochemistry and mineralogy of the Paleocene Eocene Thermal
813 Maximum (PETM): Sediment records from Egypt, India and Spain [Doctoral Dissertation]: Université
814 de Lausanne, 195 p.
- 815 Kısakürek, B., James, R.H., and Harris, N.B.W., 2005, Li and $\delta^7\text{Li}$ in Himalayan rivers: Proxies for silicate
816 weathering? *Earth and Planetary Science Letters*, v. 237, p. 387–401, doi:10.1016/j.epsl.2005.07.019.
- 817 Krause, A.J., Sluijs, A., Van Der Ploeg, R., Lenton, T.M., and Pogge Von Strandmann, P.A.E., 2023, Enhanced
818 clay formation key in sustaining the Middle Eocene Climatic Optimum: *Nature Geoscience*, v. 16, p.
819 730–738, doi:10.1038/s41561-023-01234-y.
- 820 Kump, L.R., and Arthur, M.A., 1997, Global Chemical Erosion during the Cenozoic: Weatherability Balances
821 the Budgets, *in* Ruddiman, W.F. ed., *Tectonic Uplift and Climate Change*, Boston, MA, Springer US,
822 p. 399–426, doi:10.1007/978-1-4615-5935-1_18.
- 823 Kump, L.R., Brantley, S.L., and Arthur, M.A., 2000, Chemical Weathering, Atmospheric CO_2 , and Climate:
824 Annual Review of Earth and Planetary Sciences, v. 28, p. 611–667,
825 doi:10.1146/annurev.earth.28.1.611.
- 826 Li, G., and West, A.J., 2014, Evolution of Cenozoic seawater lithium isotopes: Coupling of global denudation
827 regime and shifting seawater sinks: *Earth and Planetary Science Letters*, v. 401, p. 284–293,
828 doi:10.1016/j.epsl.2014.06.011.
- 829 Liu, C.-Y., Wilson, D.J., Hathorne, E.C., Xu, A., and Pogge Von Strandmann, P.A.E., 2023, The influence of
830 river-derived particles on estuarine and marine elemental cycles: Evidence from lithium isotopes:
831 *Geochimica et Cosmochimica Acta*, v. 361, p. 183–199, doi:10.1016/j.gca.2023.08.015.
- 832 Maffre, P., Godd ris, Y., Vigier, N., Moquet, J.-S., and Carretier, S., 2020, Modelling the riverine $\delta^7\text{Li}$
833 variability throughout the Amazon Basin: *Chemical Geology*, v. 532, p. 119336,
834 doi:10.1016/j.chemgeo.2019.119336.
- 835 Maher, K., and Von Blanckenburg, F., 2023, The circular nutrient economy of terrestrial ecosystems and the
836 consequences for rock weathering: *Frontiers in Environmental Science*, v. 10, p. 1066959,
837 doi:10.3389/fenvs.2022.1066959.
- 838 Mattauer, M., and Henry, J., 1974, Pyrenees: Special Publications, v. 4, no.1, p. 3–21.
- 839 McNerney, F.A., and Wing, S.L., 2011, The Paleocene-Eocene Thermal Maximum: A Perturbation of Carbon
840 Cycle, Climate, and Biosphere with Implications for the Future: *Annual Review of Earth and Planetary*
841 *Sciences*, v. 39, p. 489–516, doi:10.1146/annurev-earth-040610-133431.
- 842 Meunier, A., 2005, *Clays*: Berlin ; New York, Springer, 472 p.
- 843 Misra, S., and Froelich, P.N., 2012, Lithium Isotope History of Cenozoic Seawater: Changes in Silicate
844 Weathering and Reverse Weathering: *Science*, v. 335, p. 818–823, doi:10.1126/science.1214697.
- 845 Moore, D.M., and Reynolds, R.C., 1992, *Moore, Reynolds 1997_X-Ray Diffraction.pdf*: New York, Oxford
846 University Press, 401 p.
- 847 Moulton, K.L., West, J., and Berner, R.A., 2000, Solute flux and mineral mass balance approaches to the
848 quantification of plant effects on silicate weathering: v. 300, p. 539–570.
- 849 Mu oz, J.A., 1992, Evolution of a continental collision belt: ECORS-Pyrenees crustal balanced cross-section, *in*
850 McClay, K.R. ed., *Thrust Tectonics*, Dordrecht, Springer Netherlands, p. 235–246, doi:10.1007/978-
851 94-011-3066-0_21.
- 852 Murray, J., and Jagoutz, O., 2024, Palaeozoic cooling modulated by ophiolite weathering through organic
853 carbon preservation: *Nature Geoscience*, v. 17, p. 88–93, doi:10.1038/s41561-023-01342-9.

- 854 Pistiner, J.S., and Henderson, G.M., 2003, Lithium-isotope fractionation during continental weathering
855 processes: *Earth and Planetary Science Letters*, v. 214, p. 327–339, doi:10.1016/S0012-
856 821X(03)00348-0.
- 857 Pogge von Strandmann, P.A.E., Cosford, L.R., Liu, C.-Y., Liu, X., Krause, A.J., Wilson, D.J., He, X., McCoy-
858 West, A.J., Gislason, S.R., and Burton, K.W., 2023, Assessing hydrological controls on the lithium
859 isotope weathering tracer: *Chemical Geology*, v. 642, p. 121801, doi:10.1016/j.chemgeo.2023.121801.
- 860 Pogge von Strandmann, P.A.E.P.V., Dellinger, M., and West, A.J., 2021a, *Lithium Isotopes: A Tracer of Past
861 and Present Silicate Weathering*: Cambridge University Press, doi:10.1017/9781108990752.
- 862 Pogge Von Strandmann, P.A.E., Fraser, W.T., Hammond, S.J., Tarbuck, G., Wood, I.G., Oelkers, E.H., and
863 Murphy, M.J., 2019, Experimental determination of Li isotope behaviour during basalt weathering:
864 *Chemical Geology*, v. 517, p. 34–43, doi:10.1016/j.chemgeo.2019.04.020.
- 865 Pogge von Strandmann, P.A.E., Jenkyns, H.C., and Woodfine, R.G., 2013, Lithium isotope evidence for
866 enhanced weathering during Oceanic Anoxic Event 2: *Nature Geoscience*, v. 6, p. 668–672,
867 doi:10.1038/ngeo1875.
- 868 Pogge von Strandmann, P.A.E., Jones, M.T., West, A.J., Murphy, M.J., Stokke, E.W., Tarbuck, G., Wilson,
869 D.J., Pearce, C.R., and Schmidt, D.N., 2021b, Lithium isotope evidence for enhanced weathering and
870 erosion during the Paleocene-Eocene Thermal Maximum: *Science Advances*, v. 7, p. eabh4224,
871 doi:10.1126/sciadv.abh4224.
- 872 Pogge von Strandmann, P.A.E., Kasemann, S.A., and Wimpenny, J.B., 2020, Lithium and Lithium Isotopes in
873 Earth's Surface Cycles: v. 16, p. 253–258, doi:10.2138/gselements.16.4.253.
- 874 Porder, S., 2019, How Plants Enhance Weathering and How Weathering is Important to Plants: *Elements*, v. 15,
875 p. 241–246, doi:10.2138/gselements.15.4.241.
- 876 Presti, M., and Michalopoulos, P., 2008, Estimating the contribution of the authigenic mineral component to the
877 long-term reactive silica accumulation on the western shelf of the Mississippi River Delta: *Continental
878 Shelf Research*, v. 28, p. 823–838, doi:10.1016/j.csr.2007.12.015.
- 879 Prieur, M. et al., 2025, Climate Control on Erosion: Evolution of Sediment Flux From Mountainous Catchments
880 During a Global Warming Event, PETM, Southern Pyrenees, Spain: *Geophysical Research Letters*, v.
881 52, p. e2024GL112404, doi:10.1029/2024GL112404.
- 882 Prieur, M., Whittaker, A.C., Nuriel, P., Jaimes-Gutierrez, R., Garzanti, E., Roigé, M., Sømme, T.O.,
883 Schlunegger, F., and Castellort, S., 2024, Fingerprinting enhanced floodplain reworking during the
884 Paleocene–Eocene Thermal Maximum in the Southern Pyrenees (Spain): Implications for channel
885 dynamics and carbon burial: *Geology*, v. 52, p. 651–655, doi:10.1130/G52180.1.
- 886 Puigdefbregas, C., and Souquet, P., 1986, Tecto-sedimentary cycles and depositional sequences of the Mesozoic
887 and Tertiary from the Pyrenees: v. 129, p. 173–203.
- 888 Pujalte, V., Baceta, J.I., and Schmitz, B., 2015, A massive input of coarse-grained siliciclastics in the Pyrenean
889 Basin during the PETM: the missing ingredient in a coeval abrupt change in hydrological regime:
890 *Climate of the Past*, v. 11, p. 1653–1672, doi:10.5194/cp-11-1653-2015.
- 891 Pujalte, V., Robador, A., Aitor Payros, and Samsó, J.M., 2016, A siliciclastic braid delta within a lower
892 Paleogene carbonate platform (Ordessa-Monte Perdido National Park, southern Pyrenees, Spain):
893 Record of the Paleocene–Eocene Thermal Maximum perturbation: *Palaeogeography,
894 Palaeoclimatology, Palaeoecology*, v. 459, p. 453–470, doi:10.1016/j.palaeo.2016.07.029.
- 895 Pujalte, V., and Schmitz, B., 2005, Revisión de la estratigrafía del Grupo Tremp («Garumniense»), Cuenca de
896 Tremp-Graus, Pirineos meridionales):

- 897 Pujalte, V., Schmitz, B., and Baceta, J.I., 2014, Sea-level changes across the Paleocene–Eocene interval in the
898 Spanish Pyrenees, and their possible relationship with North Atlantic magmatism: *Palaeogeography,*
899 *Palaeoclimatology, Palaeoecology*, v. 393, p. 45–60, doi:10.1016/j.palaeo.2013.10.016.
- 900 Pujalte, V., Schmitz, B., Baceta, J.I., Orue-Etxebarria, X., Bernaola, G., Dinarès-Turell, J., Payros, A.,
901 Apellaniz, E., and Caballero, F., 2009, Correlation of the Thanetian-Ilerdian turnover of larger
902 foraminifera and the Paleocene-Eocene thermal maximum: confirming evidence from the Campo area
903 (Pyrenees, Spain): *Geologica Acta*, v. 7.
- 904 Ramos, E.J. et al., 2024, Competition or collaboration: Clay formation sets the relationship between silicate
905 weathering and organic carbon burial in soil: *Earth and Planetary Science Letters*, v. 628, p. 118584,
906 doi:10.1016/j.epsl.2024.118584.
- 907 Ramos, E.J. et al., 2022, Swift Weathering Response on Floodplains During the Paleocene-Eocene Thermal
908 Maximum: *Geophysical Research Letters*, v. 49, doi:10.1029/2021GL097436.
- 909 Raymo, M.E., and Ruddiman, W.F., 1992, Tectonic forcing of late Cenozoic climate: *Nature*, v. 359, p. 117–
910 122, doi:10.1038/359117a0.
- 911 Riebe, C.S., Kirchner, J.W., and Finkel, R.C., 2004, Erosional and climatic effects on long-term chemical
912 weathering rates in granitic landscapes spanning diverse climate regimes: *Earth and Planetary Science*
913 *Letters*, v. 224, p. 547–562, doi:10.1016/j.epsl.2004.05.019.
- 914 Roest, W.R., and Srivastava, S.P., 1991, Kinematics of the plate boundaries between Eurasia, Iberia, and Africa
915 in the North Atlantic from the Late Cretaceous to the present: *Geology*, v. 19, p. 613,
916 doi:10.1130/0091-7613(1991)019<0613:KOTPB>2.3.CO;2.
- 917 Rosenbaum, G., Lister, G.S., and Duboz, C., 2002, Reconstruction of the tectonic evolution of the western
918 Mediterranean since the Oligocene: *Journal of the Virtual Explorer*, v. 08,
919 doi:10.3809/jvirtex.2002.00053.
- 920 Roure, F., Choukroune, P., Berastegui, X., Munoz, J.A., Villien, A., Matheron, P., Bareyt, M., Seguret, M.,
921 Camara, P., and Deramond, J., 1989, Ecore deep seismic data and balanced cross sections: Geometric
922 constraints on the evolution of the Pyrenees: *Tectonics*, v. 8, p. 41–50, doi:10.1029/TC008i001p00041.
- 923 Rush, W.D., Kiehl, J.T., Shields, C.A., and Zachos, J.C., 2021, Increased frequency of extreme precipitation
924 events in the North Atlantic during the PETM: Observations and theory: *Palaeogeography,*
925 *Palaeoclimatology, Palaeoecology*, v. 568, p. 110289, doi:10.1016/j.palaeo.2021.110289.
- 926 Rush, W., Zachos, J., Blackburn, T., and Pogge Von Strandmann, P.A.E., 2025, Continuous Sediment Sourcing
927 and Changes in Weathering During the PETM in the Salisbury Embayment: *Paleoceanography and*
928 *Paleoclimatology*, v. 40, p. e2025PA005116, doi:10.1029/2025PA005116.
- 929 Schmitz, B., and Pujalte, V., 2007, Abrupt increase in seasonal extreme precipitation at the Paleocene-Eocene
930 boundary: *Geology*, v. 35, p. 215, doi:10.1130/G23261A.1.
- 931 Schmitz, B., and Pujalte, V., 2003, Sea-level, humidity, and land-erosion records across the initial Eocene
932 thermal maximum from a continental-marine transect in northern Spain: *Geology*, v. 31, p. 689,
933 doi:10.1130/G19527.1.
- 934 Schmitz, B., Pujalte, V., and Nunhez-Betelu, K., 2001, Climate and sea-level perturbations during the Initial
935 Eocene Thermal Maximum: evidence from siliciclastic units in the Basque Basin (Ermua, Zumaia and
936 Trabakua Pass), northern Spain: *Palaeogeography, Palaeoclimatology, Palaeoecology* 165, p. 299–320.
- 937 Spangenberg, J.E., 2006, Hydrocarbon Biomarkers in the Topla-Mezica Zinc-Lead Deposits, Northern
938 Karavanke/Drau Range, Slovenia: *Paleoenvironment at the Site of Ore Formation*:
- 939 Spangenberg, J.E., and Zufferey, V., 2019, Carbon isotope compositions of whole wine, wine solid residue, and
940 wine ethanol, determined by EA/IRMS and GC/C/IRMS, can record the vine water status—a

- 941 comparative reappraisal: *Analytical and Bioanalytical Chemistry*, v. 411, p. 2031–2043,
942 doi:10.1007/s00216-019-01625-4.
- 943 Środoń, J., 2001, Quantitative X-Ray Diffraction Analysis of Clay-Bearing Rocks from Random Preparations:
944 Clays and Clay Minerals, v. 49, p. 514–528, doi:10.1346/CCMN.2001.0490604.
- 945 Tanaka, T. et al., 2000, JNdi-1: a neodymium isotopic reference in consistency with LaJolla neodymium:
946 *Chemical Geology*, v. 168, p. 279–281, doi:10.1016/S0009-2541(00)00198-4.
- 947 Teixell, A., Labaume, P., and Lagabrielle, Y., 2016, The crustal evolution of the west-central Pyrenees revisited:
948 Inferences from a new kinematic scenario: *Comptes Rendus. Géoscience*, v. 348, p. 257–267,
949 doi:10.1016/j.crte.2015.10.010.
- 950 Thiry, M., 2000, Palaeoclimatic interpretation of clay minerals in marine deposits: an outlook from the
951 continental origin: *Earth-Science Reviews*, v. 49, p. 201–221, doi:10.1016/S0012-8252(99)00054-9.
- 952 Tofelde, S., Bernhardt, A., Guerit, L., and Romans, B.W., 2021, Times Associated With Source-to-Sink
953 Propagation of Environmental Signals During Landscape Transience: *Frontiers in Earth Science*, v. 9,
954 p. 628315, doi:10.3389/feart.2021.628315.
- 955 Tremblin, M. et al., 2022, Mercury enrichments of the Pyrenean foreland basins sediments support enhanced
956 volcanism during the Paleocene-Eocene thermal maximum (PETM): *Global and Planetary Change*, v.
957 212, p. 103794, doi:10.1016/j.gloplacha.2022.103794.
- 958 Velde, B., and Meunier, A., 2008, *The Origin of Clay Minerals in Soils and Weathered Rocks*: Berlin,
959 Heidelberg, Springer Berlin Heidelberg, doi:10.1007/978-3-540-75634-7.
- 960 Vigier, N., Decarreau, A., Millot, R., Carignan, J., Petit, S., and France-Lanord, C., 2008, Quantifying Li
961 isotope fractionation during smectite formation and implications for the Li cycle: *Geochimica et*
962 *Cosmochimica Acta*, v. 72, p. 780–792, doi:10.1016/j.gca.2007.11.011.
- 963 Vimperc, L. et al., 2023, Carbon isotope and biostratigraphic evidence for an expanded Paleocene–Eocene
964 Thermal Maximum sedimentary record in the deep Gulf of Mexico: *Geology*, doi:10.1130/G50641.1.
- 965 Walker, J.C.G., Hays, P.B., and Kasting, J.F., 1981, A negative feedback mechanism for the long-term
966 stabilization of Earth's surface temperature: *Journal of Geophysical Research: Oceans*, v. 86, p. 9776–
967 9782, doi:10.1029/JC086iC10p09776.
- 968 Wei, G.-Y., Pohl, A., Jiang, S., Zhang, H., Wang, W., A. E. Pogge Von Strandmann, P., Maffre, P., Xiong, G.,
969 Shen, S., and Zhang, F., 2025, Changes in continental weathering regimes inhibited global marine
970 deoxygenation during the Paleocene–Eocene thermal maximum: *Nature Communications*, v. 16, p.
971 9163, doi:10.1038/s41467-025-64217-0.
- 972 Weis, D., Kieffer, B., Maerschalk, C., Pretorius, W., and Barling, J., 2005, High-precision Pb-Sr-Nd-Hf isotopic
973 characterization of USGS BHVO-1 and BHVO-2 reference materials: *Geochemistry, Geophysics,*
974 *Geosystems*, v. 6, p. 2004GC000852, doi:10.1029/2004GC000852.
- 975 West, A., Galy, A., and Bickle, M., 2005, Tectonic and climatic controls on silicate weathering: *Earth and*
976 *Planetary Science Letters*, v. 235, p. 211–228, doi:10.1016/j.epsl.2005.03.020.
- 977 Westerhold, T., Röhl, U., McCarren, H.K., and Zachos, J.C., 2009, Latest on the absolute age of the Paleocene–
978 Eocene Thermal Maximum (PETM): New insights from exact stratigraphic position of key ash layers
979 +19 and –17: *Earth and Planetary Science Letters*, v. 287, p. 412–419, doi:10.1016/j.epsl.2009.08.027.
- 980 Wilson, D.J., Pogge von Strandmann, P.A.E., White, J., Tarbuck, G., Marca, A.D., Atkinson, T.C., and Hopley,
981 P.J., 2021, Seasonal variability in silicate weathering signatures recorded by Li isotopes in cave drip-
982 waters: *Geochimica et Cosmochimica Acta*, v. 312, p. 194–216, doi:10.1016/j.gca.2021.07.006.

- 983 Winnick, M.J., Druhan, J.L., and Maher, K., 2022, Weathering intensity and lithium isotopes: A reactive
984 transport perspective: *American Journal of Science*, v. 322, p. 647–682, doi:10.2475/05.2022.01.
- 985 Wise, S.W., Smellie, J., Aghib, F., Jarrard, R., and Krissek, L., 2001, Authigenic Smectite Clay Coats in CRP-3
986 Drillcore, Victoria Land Basin, Antarctica, as a Possible Indicator of Fluid Flow: A Progress Report: ,
987 p. 281–298.
- 988 Xu, Z., Li, T., Li, G., Hedding, D.W., Wang, Y., Gou, L.-F., Zhao, L., and Chen, J., 2022, Lithium isotopic
989 composition of soil pore water: Responses to evapotranspiration: *Geology*, v. 50, p. 194–198,
990 doi:10.1130/G49366.1.
- 991 Zachos, J.C., Dickens, G.R., and Zeebe, R.E., 2008, An early Cenozoic perspective on greenhouse warming and
992 carbon-cycle dynamics: *Nature*, v. 451, p. 279–283, doi:10.1038/nature06588.
- 993 Zachos, J.C., Wara, M.W., Bohaty, S., Delaney, M.L., Petrizzo, M.R., Brill, A., Bralower, T.J., and Premoli-
994 Silva, I., 2003, A Transient Rise in Tropical Sea Surface Temperature During the Paleocene-Eocene
995 Thermal Maximum: *Science*, v. 302, p. 1551–1554, doi:10.1126/science.1090110.
- 996 Zeebe, R.E., Ridgwell, A., and Zachos, J.C., 2016, Anthropogenic carbon release rate unprecedented during the
997 past 66 million years: *Nature Geoscience*, v. 9, p. 325–329, doi:10.1038/ngeo2681.
- 998 Zhang, F., Dellinger, M., Hilton, R.G., Yu, J., Allen, M.B., Densmore, A.L., Sun, H., and Jin, Z., 2022,
999 Hydrological control of river and seawater lithium isotopes: *Nature Communications*, v. 13, p. 3359,
1000 doi:10.1038/s41467-022-31076-y.
- 1001